HHS Public Access

Author manuscript

Cell Metab. Author manuscript; available in PMC 2023 December 06.

Published in final edited form as:

Cell Metab. 2022 December 06; 34(12): 1932–1946.e7. doi:10.1016/j.cmet.2022.09.019.

The rheumatoid arthritis drug auranofin lowers leptin levels and exerts anti-diabetic effects in obese mice

Aaron R. Cox[1,*], **Peter M. Masschelin**[1,2], **Pradip K. Saha**[1], **Jessica B. Felix**[1,2], **Robert Sharp**[1], **Zeqin Lian**[3], **Yan Xia**[2], **Natasha Chernis**[1], **David A. Bader**[2], **Kang Ho Kim**[2,4], **Xin Li**[5], **Jun Yoshino**[6], **Xin Li**[1], **Gang Li**[5], **Zheng Sun**[1,2], **Huaizhu Wu**[3], **Cristian Coarfa**[2,7], **David D. Moore**[2,8], **Samuel Klein**[6], **Kai Sun**[5], **Sean M. Hartig**[1,2,9,*]

[1]Division of Diabetes, Endocrinology, and Metabolism, Department of Medicine, Baylor College of Medicine, Houston, TX

[2]Department of Molecular and Cellular Biology, Baylor College of Medicine, Houston, TX

[3]Cardiovascular Research, Department of Medicine, Baylor College of Medicine, Houston, TX

[4]Department of Anesthesiology, UTHealth McGovern Medical School, Houston, TX

[5]Center for Metabolic and Degenerative Diseases, the Brown Foundation Institute of Molecular Medicine for the Prevention of Human Diseases, University of Texas Health Science Center at Houston, Houston, TX

[6]Center for Human Nutrition, Washington University School of Medicine, St. Louis, MO

[7]Dan L. Duncan Comprehensive Cancer Center, Baylor College of Medicine, Houston, TX

[8]Department of Nutritional Sciences and Toxicology, University of California Berkeley, Berkeley, CA

[9]Lead contact

SUMMARY

Low grade, sustained inflammation in white adipose tissue (WAT) characterizes obesity and coincides with type 2 diabetes mellitus (T2DM). However, pharmacological targeting of inflammation lacks durable therapeutic effects in insulin resistant conditions. Through a computational screen, we discovered the FDA-approved rheumatoid arthritis drug auranofin improved insulin sensitivity and normalized obesity-associated abnormalities, including hepatic

[*]Correspondence should be addressed to A.R.C. or S.M.H. racox@bcm.edu or hartig@bcm.edu.

AUTHOR CONTRIBUTIONS

A.R.C. and S.M.H. conceptualized the study. A.R.C, S.M.H., and the remaining authors performed critical experiments in mice and/or contributed to the interpretation of metabolic phenotypes and biochemical outcomes. A.R.C. and S.M.H. wrote the manuscript with editorial input from all authors. S.M.H. is the guarantor of this work and, as such, had full access to all the data in the study and takes responsibility for the integrity of the data and the accuracy of the data analysis.

DECLARATION OF INTERESTS

The authors declare no competing interests.

steatosis and hyperinsulinemia in mouse models of T2DM. We also discovered auranofin accumulation in WAT depleted inflammatory responses to high fat diet without altering body composition in obese wild-type mice. Surprisingly, elevated leptin levels and blunted beta-adrenergic receptor activity achieved by leptin receptor deletion abolished the anti-diabetic effects of auranofin. These experiments also revealed the metabolic benefits of leptin reduction were superior to immune impacts of auranofin in WAT. Our studies uncover important metabolic properties of anti-inflammatory treatments and contribute to the notion that leptin reduction in the periphery can be accomplished to treat obesity and T2DM.

Graphical Abstract

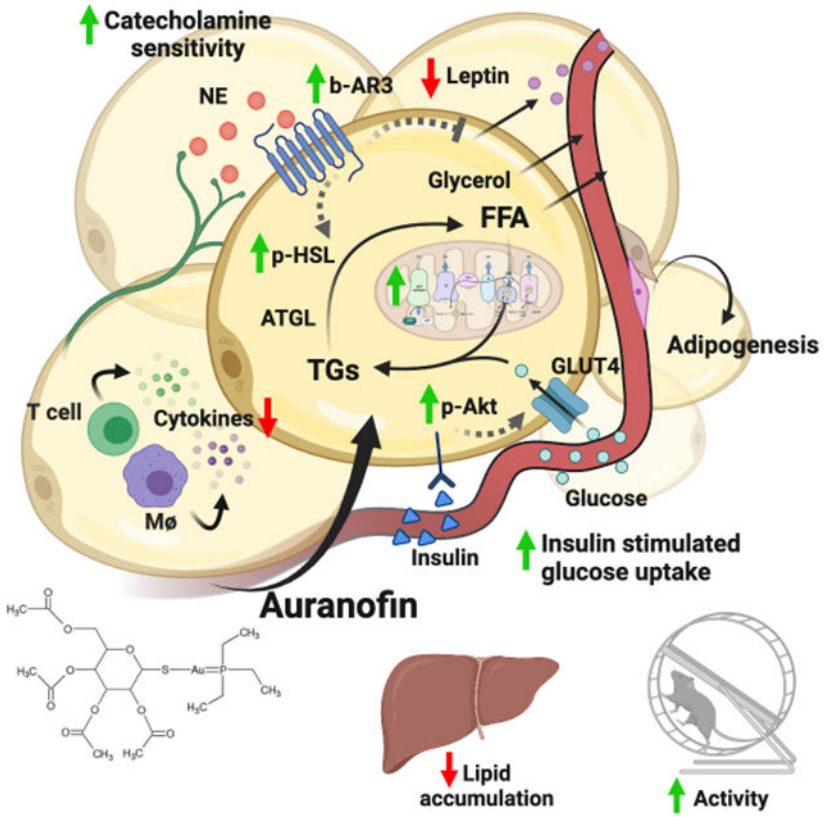

IN BRIEF

The FDA-approved rheumatoid arthritis drug auranofin accumulates in white adipose tissue, improves insulin sensitivity, and normalizes fatty liver disease in obesity. Beta-adrenergic receptor regulation of leptin secretion generates metabolic benefits superior to anti-inflammatory effects. Consequently, studies of auranofin reinforce partial leptin reduction represents a relevant method for treating obesity.

Keywords

insulin sensitivity; inflammation; leptin reduction; auranofin; obesity

INTRODUCTION

The obesity epidemic contributes to the increased health burden of chronic inflammatory conditions, including insulin resistance, type 2 diabetes mellitus (T2DM), fatty liver, and cardiovascular disease (Afshin et al., 2017). Among the clinical relationships proposed to explain how excess body weight causes insulin resistance, WAT inflammation remains one of the most debated incident conditions associated with obesity and its co-morbidities (Klein et al., 2022). Many studies demonstrate WAT inflammation causes insulin resistance in rodents (Rohm et al., 2022) and widely used anti-diabetic drugs exert anti-inflammatory effects as part of their therapeutic activity (Isoda et al., 2006; Soccio et al., 2014). Although WAT inflammation is one conserved response linking obesity to insulin resistance and T2DM, targeting immune components of obesity has proved elusive, and broad anti-inflammatory strategies lack clinical efficacy (Goldfine et al., 2013; Goldfine et al., 2010; Ofei et al., 1996). Nonetheless, there is a definitive association between inflammation in WAT and insulin resistance in humans and rodents.

We demonstrated enforced expression of the microRNA *miR-30a* in subcutaneous fat tissues caused anti-diabetic effects in mice (Koh et al., 2018). *miR-30a* opposed actions of macrophage and T cell cytokines in WAT, suggesting important roles for *miR-30a* in defending adipocytes against pro-inflammatory signals. Notably, we also reported *miR-30a* expression in WAT corresponds with insulin sensitivity in obese mice and people. Our findings support the concept that sustained *miR-30a* expression may uncouple obesity from its co-morbidities. The present study grew from computational methods motivated by the idea that we can repurpose FDA-approved therapies that generate *miR-30a*-like effects for treating obesity.

RESULTS

A computational approach identifies metabolic benefits of auranofin

We hypothesized small molecules that drive immune and metabolic changes similar to ectopic *miR-30a* (Adv-*miR-30a*) expression in WAT generate anti-diabetic effects. To explore this hypothesis, we used the Broad Connectivity Map (Lamb et al., 2006) to perform an *in silico* screen for small molecules with gene expression signatures resembling Adv-*miR-30a* in WAT (Figure 1A; Table S1-S2). Through this process, we identified the gold salt auranofin as a compound with a highly similar gene expression pattern to Adv-*miR-30a*. Notably, compounds inversely correlated with the Adv-*miR-30a* signature included inhibitors of the PI3K pathway and insulin action, including wortmannin (Huang et al., 2004), PIK-90 (Knight et al., 2006), BMS-536924 (Wittman et al., 2005) and MK-2206 (Tan et al., 2011).

In addition to effects on immune responses, auranofin (Ridaura) intrigued us because it is an FDA-approved, orally available medication for treating rheumatoid arthritis (RA), an inflammatory condition often coupled with hyperglycemia, insulin resistance, and the comorbidities of T2DM (Giles et al., 2018). In persons receiving chrysotherapy for RA, traces of gold can be found in numerous tissues except for the brain (Gottlieb et al., 1972; Vernon-Roberts et al., 1976). Therefore, we administered auranofin i.p. to obese

mice and defined the tissue distribution of auranofin. Using mass spectrometry, we found auranofin accumulated in epididymal WAT (eWAT) and inguinal fat compartments (Figure 1B) compared to all other tissues examined.

To examine cell-autonomous impacts of auranofin, we used differentiated adipocytes generated from the inguinal WAT (iWAT) stromal vascular fraction (SVF) of wild-type mice. First, we modeled obesity-induced WAT inflammation by treating SVF-derived adipocytes with interferon gamma (IFNγ) for 24 h (Wentworth et al., 2017). Chronic IFNγ treatment increased mRNA levels of pro-inflammatory targets, including *Stat1, Isg15, Tnfa,* and *Irf1* (Figure S1A). These effects were prevented entirely by co-treatment with auranofin. Auranofin-treated cells also exhibited more densely packed mitochondria (Figure S1B), contributing to greater respiratory capacity (Figure S1C). Likewise, auranofin increased expression of metabolic genes *Ucp1, Pgc1a, Cycs, Cpt1b,* and *Pdk4* that define brown and beige adipocyte functions (Figure S1D).

To explore additional functional similarities of auranofin and *miR-30a,* we then measured gene expression responses of human adipocytes treated with *miR-30a* mimics, auranofin, or appropriate controls. Consistent with the mouse SVF studies (Figure S1B), human adipocytes treated with auranofin showed more dense MitoTracker staining (Figure S2A), which correlated with higher expression of the adipogenic genes *ADIPOQ, PGC1a, UCP1,* and *miR-30a* itself (Figure S2B). As expected, auranofin also suppressed pro-inflammatory target genes of the transcription factor STAT1 (Figure S2B). Intriguingly, the effects of auranofin or *miR-30a* overexpression on metabolic and inflammatory genes in human adipocytes were mostly indistinguishable (Figure S2B). To define any shared anti-inflammatory effects of auranofin and *miR-30a,* we transfected human adipocytes with control or *miR-30a* mimics followed by pre-treatment with auranofin before exposure to IFNγ. IFNγ potently stimulated *STAT1* and *ISG15* while blunting expression of *miR-30a* and genes critical for insulin sensitivity (*ADIPOQ, PGC1a, PPARG*). Auranofin or *miR-30a* pre-treatments blocked pro-inflammatory gene induction and allowed *PGC1a, UCP1,* and *ADIPOQ* expression to resist suppressive effects of IFNγ (Figure S2C). Combined *miR-30a* and auranofin conditions did not additively alter gene expression, suggesting shared pathway effects. Collectively, these data demonstrate auranofin exhibits similar functions as *miR-30a* in that it disrupts inflammatory signals and supports metabolic changes known to improve insulin sensitivity.

With the ultimate goal of identifying drugs like auranofin to treat T2DM, we performed dose-escalation studies in obese mice to identify a tolerable treatment regimen. Wild-type mice fed high-fat diet (HFD) for 12 weeks were i.p. injected with doses of auranofin three days per week (Monday/Wednesday/Friday) for one month and then administered an insulin tolerance test (ITT). We quickly learned the published 10 mg/kg treatment regimens (Fiskus et al., 2014) and two lower doses caused unreported malaise and dramatic weight loss (Figure 1C). ITT (Figure 1D) and attendant area under the curve (Figure 1E) calculations showed significantly greater responsiveness to insulin in all auranofin-treated groups compared to vehicle controls. To address the possibility the weight loss observed at higher doses derived from hypophagia, we performed a fast-refeeding experiment. After an overnight fast, mice were injected with auranofin or vehicle thirty minutes before re-feeding

(Figure 1F). Control mice responded immediately to food reintroduction and continued to eat during the follow-up period. In contrast, mice receiving the higher doses of auranofin showed food aversion and exhibited noticeable malaise, suggesting auranofin levels above 1 mg/kg caused measurable distress. Mice tolerated the 1 mg/kg dose well, and we observed no effects on food intake or gross behaviors. Importantly, allometric scaling indicated the 1 mg/kg dose three days/week approached doses used clinically (maximum 9 mg/day). These data demonstrate effective doses of auranofin administered at levels ten-fold lower than previous studies (Fiskus et al., 2014) and bio-equivalent to humans improved insulin sensitivity and furnished previously unrecognized therapeutic benefits in obesity.

We built upon experiments at the 1 mg/kg dose to determine whether auranofin improves the metabolic and inflammatory profile of obesity. Magnetic resonance imaging (MRI) measurements of fat and lean mass established body composition of auranofin and vehicle groups were equivalent (Figure 1G), despite modest reductions in body weight (Figure 1C). Using Comprehensive Lab Animal Monitoring System (CLAMS) cages, we found auranofin treatment in obese mice did not demonstrably impact food intake (Figure 1H) or respiratory exchange ratio (RER, Figure 1I). However, auranofin treatment in obese mice led to higher physical activity in the dark cycle (Figure 1J).

Auranofin exerts anti-Diabetic effects in mice with diet-induced obesity

We expanded the earlier studies to comprehensively understand the impacts of auranofin on glucose metabolism. Auranofin treatment significantly improved insulin (Figure 2A) and glucose tolerance (Figure 2B) in obese mice and corrected hyperinsulinemia, HOMA-IR, and glucose-stimulated insulin secretion (Figure 2C). Of note, auranofin reduced serum dipeptidyl-peptidase-4 (Figure 2D), a liver-derived inflammatory protein that circulates at high levels in diabetic mice and people (Mulvihill and Drucker, 2014). In agreement with improved insulin sensitivity, auranofin reduced liver weight (Figure 2E) and hepatic triglyceride accumulation (Figure 2F). RNA-seq established auranofin reduced the activity of several metabolic pathways known to cluster with fatty liver disease, including glycolysis and gluconeogenesis (Figure 2G), and suppressed expression of many genes involved in lipogenesis (*Khk, Pdk1, Tkt, Tkfc*). We next asked whether insulin sensitivity changes in auranofin-treated mice reflected improved insulin signaling (Figure 2H). Despite the fatty liver reduction, auranofin only increased insulin-dependent Akt phosphorylation in eWAT. To better understand the insulin sensitivity phenotype, we performed hyperinsulinemic-euglycemic clamps in unrestrained HFD-fed mice (Figure 2I). We observed increases in the glucose infusion rate (GIR) required to maintain euglycemia in auranofin-treated mice compared to controls, supporting the improved insulin sensitivity phenotype. The GIR was increased 2.4-fold in auranofin-treated mice, an effect size equivalent to diabetes drugs used in preclinical studies (Lu et al., 2011; Reilly et al., 2013; Samms et al., 2021). The primary factor contributing to the increased GIR was elevated whole-body glucose utilization, with pronounced effects observed in eWAT but not skeletal muscle. While basal glucose production by the liver was decreased by auranofin, there was no significant difference in the ability of insulin to suppress endogenous glucose production. These findings suggest the enhanced insulin sensitivity caused by auranofin accumulation in eWAT is primarily due to greater glucose uptake and not decreased glucose production. Together, these data

demonstrate auranofin increased insulin sensitivity in tissue-specific ways and improved the metabolic phenotype of obese mice.

Next, we studied the effect of auranofin on glucose homeostasis in lean mice. Eighteen-week-old wild-type mice were given 1 mg/kg auranofin three days per week (Monday/Wednesday/Friday) for one month, followed by metabolic phenotyping. We observed no malaise or body composition effects in lean mice receiving auranofin compared to vehicle controls (Figure S3A-C). Insulin (Figure S3D) and glucose (Figure S3E) tolerance tests performed on lean mice also showed no effect of drug. Fasting insulin levels were equivalent between auranofin and control mice (Figure S3F). These data argue auranofin actions require obesity.

Accumulation of auranofin in WAT depletes inflammatory responses of obesity

During sustained HFD, obesity initiates low-grade inflammation in WAT that coincides with insulin resistance and T2DM (Lumeng et al., 2007; Weisberg et al., 2003). Drug accumulation (Figure 1B) and enhanced insulin action in eWAT (Figure 2H-I) suggested auranofin may influence changes in the eWAT that govern local tissue inflammation. Histology and quantitative image analysis revealed adipocytes from auranofin-treated mice were significantly smaller (Figure 3A), favoring reduced adipocyte hypertrophy (Jeffery et al., 2016). To identify biologically cohesive gene programs of auranofin accumulation in the eWAT of obese mice, we used RNA-Seq. These efforts uncovered clear signatures that explained the impacts of auranofin in the eWAT. Consistent with smaller adipocytes, qPCR validation studies (Figure 3B) uncovered that auranofin increased expression of adipogenesis markers (*Adipoq, Glut4, Acaca, Scd1*) and concurrently depleted levels of preadipocyte genes (*Prrx1, Fsp1*). Moreover, Gene Set Enrichment Analysis (GSEA) indicated auranofin elevated levels of genes found in central metabolic pathways, including oxidative phosphorylation, adipogenesis, and fatty acid metabolism (Figure 3C). Not surprisingly, GSEA also demonstrated wide anti-inflammatory effects reflected by changes in marker genes of macrophages, innate immunity, and the inflammasome (Figure 3D).

To further characterize cell signaling events underpinning the metabolic and inflammatory phenotypes, we applied WAT and brown adipose tissue (BAT) samples to a reverse phase protein array (RPPA) with broad pathway coverage (Figure 3E). Auranofin imparted the most robust impacts on eWAT probes, including depletion of well-established protein markers of inflammation in the NF-kB (IKKb, p-IKK, p-IkBa, NF-kB, p-NF-kB) and JAK-STAT (p-JAK1, STAT3) signaling pathways. Blocking these pathways coincided with decreased levels of pro-inflammatory molecules (DPP4, TNFa) and chemokines (MCP1, M-CSF, RANTES) in the eWAT (Figure 3F). These data suggested decreased function of macrophages, so we performed flow cytometry using standard antibody markers on immune cells extracted from the eWAT SVF. Total macrophages labeled by F4/80 were significantly reduced with auranofin treatment (Figure 3G). Macrophage populations defined by classic surface markers after tissue digestion of the SVF were likewise indiscriminately decreased by auranofin, suggesting across-the-board depletion rather than unique targeting of CD11c+ or CD206+ immune cells.

miR-30a provides a fractional contribution to the effects of auranofin

Our previous findings (Koh et al., 2018) demonstrated *miR-30a* improved the inflammatory profile of obesity and formed the foundation to nominate auranofin as a putative anti-diabetic therapy (Figure 1A and Table S2). Because auranofin showed similar metabolic and anti-inflammatory effects as Adv-*miR-30a* in WAT, we investigated whether *miR-30a* accounted for the benefits of auranofin in obese mice. To this end, we used CRISPR/Cas9 gene editing to knock out the *miR-30a* gene in mice (Figure 4A). To determine if *miR-30a* loss resulted in compensation from other *miR-30* family members, we measured *miR-30c-2* (*miR-30c*), located 20 kb downstream of *miR-30a* on chromosome 1. *miR-30c* expression was equivalent between wild-type and *miR-30a*$^{-/-}$ across all tissues tested, which also supported on-target gene editing (Figure 4B). Despite heightened expression of pro-inflammatory genes in eWAT (Figure S4A), the *miR-30a*$^{-/-}$ mice showed no overt energy balance phenotypes during postnatal growth (Figure S4) and HFD feeding (Figure 4C-D) compared to littermate wild-type controls.

We then performed longitudinal profiling of body weight and insulin sensitivity in wild-type and *miR-30a*$^{-/-}$ mice on HFD before and after auranofin treatment. After 12 weeks of HFD, *miR-30a*$^{-/-}$ and wild-type mice were treated with auranofin (1 mg/kg) for four weeks. Both genotypes gained weight at similar rates during treatment (Figure 4E). Although glucose tolerance (Figure 4F) did not change among treatments and genotypes, auranofin improved fasting glucose (Figure 4G) and insulin sensitivity profiles (Figure 4H) equivalently in *miR-30a*$^{-/-}$ and wild-type mice. The influence of *miR-30a* on WAT inflammation (Koh et al., 2018) prompted us to assess eWAT inflammation and fibrosis in *miR-30a*$^{-/-}$ mice. Similar to the eWAT gene expression profile of *miR-30a*$^{-/-}$ mice (Figure S4A), RPPA revealed *miR-30a* ablation increased expression of pro-inflammatory NF-kB and JAK-STAT probes in eWAT compared to wild-type mice on HFD (Figure 4I). Furthermore, histological analysis of eWAT indicated *miR-30a*$^{-/-}$ mice contained more remnant CD68+ cells compared to wild-type mice after drug treatment (Figure 4J), suggesting auranofin may be ineffective towards macrophage recruitment in *miR-30a*$^{-/-}$ eWAT. However, gene expression profiling showed unremarkable changes in auranofin-sensitive inflammatory and fibrosis markers among all mice that received auranofin (Figure 4K). Overall, residual macrophage staining and gene expression studies indicate that auranofin and *miR-30a* shared some impacts on tissue-specific inflammatory effects of HFD, but whole-body metabolic phenotypes of auranofin do not require *miR-30a* expression.

Auranofin reduces serum leptin levels

WAT secretes proteins that serve as biomarkers of tissue expansion and contribute to insulin sensitivity (Sakers et al., 2022). We observed the induction of adipocyte differentiation genes by auranofin also preceded the abundance of adiponectin in the plasma (Figure 5A). Additionally, we found auranofin caused significant decreases in serum leptin (Figure 5B) and the leptin/adiponectin ratio (Figure 5C) independent of eWAT *Lep* mRNA (Figure 5D) changes in HFD-fed wild-type mice compared to controls. Leptin lowering supports hypothalamic neuron activities for energy balance in obese mice (Zhao et al., 2020; Zhao et al., 2019). In line with this idea, auranofin treatment caused small but significantly higher p-STAT3 in the arcuate, dorsomedial, and ventromedial nuclei of the hypothalamus (Figure

5E). When combined with the insulin sensitivity effects, the auranofin phenotype agreed with the beneficial effects of partial leptin reduction in obesity (Zhao et al., 2019).

The insulin sensitivity effects of auranofin require intact leptin signaling

In efforts to determine whether auranofin influenced obesity sequelae in other mouse models, we pursued experiments in leptin-deficient backgrounds that do not need HFD interventions for insulin resistance. We began with inducible leptin receptor knockout mice (*Ubc-Cre;LepR*$^{lp/lp}$; *LepR KO*), an obesity model without complications of uncontrollable diabetes observed in *db/db* mice (Cox et al., 2016). *LepR KO* mice gained ~17-19 g over four weeks after Cre activation, at which point we randomized mice to receive vehicle or auranofin. During the four-week intervention that followed, all *LepR KO* mice gained weight at equivalent rates (Figure 6A) and endpoint MRI analysis showed similar body compositions between treatments (Figure 6B-C). In contrast to observations in obese wild-type mice (Figure 2), *LepR KO* mice lacked metabolic responses to auranofin. qPCR reaffirmed *Lep* gene expression in eWAT was unaffected by auranofin (Figure 6D), but *LepR KO* eWAT expressed significantly higher levels of *Lep* compared to wild-type mice and the ensuing hyperleptinemia resisted auranofin treatment (Figure 6E). Likewise, CLAMS studies indicated comparable food intake (Figure 6F), RER (Figure 6G), and activity (Figure 6H) between vehicle and auranofin groups. Insulin (Figure 6I) and glucose tolerance (Figure 6J) tests, as well as fasting serum insulin (Figure 6K) and features of fatty liver disease (Figure 6L), were also equivalent in vehicle and auranofin-treated *LepR KO* mice. Histology (Figure 6M), along with targeted gene expression profiling (Figure 6N) and RPPA (Figure 6O), further suggested *LepR KO* lacked the wild-type anti-inflammatory responses to auranofin in eWAT. We additionally tested auranofin in leptin-deficient (*ob/ob*) mice and detected a similar resistance to auranofin (Figure S5). Thus, our enrollment of additional mouse models argued the insulin-sensitizing effects of auranofin required intact leptin signaling.

Auranofin couples leptin bioavailability with lipolytic competence in WAT

Leptin also induces lipolysis through activation of beta-adrenergic receptor (βAR) signaling in WAT, a feature largely diminished in chronic obesity and T2DM (Pirzgalska et al., 2017; Zeng et al., 2015). We revisited our RNA-seq data and found auranofin significantly increased lipolytic gene expression in the eWAT, including markedly higher levels of *Adrb3, Atgl,* and *Lipe/Hsl* (Figure 3C). To follow up on these observations, we performed a series of experiments to test the impact of auranofin on the leptin-*Adrb3* axis. Auranofin induced expression of *Adrb3* in wild-type but not hyperleptinemic *LepR KO* eWAT (Figure 7A). Notably, WAT from metabolically unhealthy obese people (Cifarelli et al., 2020) exhibited elevated serum leptin (Figure 7B) coupled with blunted expression of lipolysis genes (*ADRB3, LIPE/HSL*) compared to healthy controls (Figure 7C). These data support the notion that lipolytic responses of eWAT may be impaired in the absence of intact leptin signaling. Next, we explored whether auranofin converts the enrichment of metabolic genes to functional changes in eWAT lipolysis and fatty acid metabolism. *In vivo,* auranofin treatment increased fasting serum free fatty acids (FFA) in wild-type mice but not in *LepR KO* mice (Figure 7D). In an orthogonal approach to determine whether auranofin influenced fatty acid disposal, we measured oxygen consumption rates (OCR) in eWAT of wild-type

and *LepR KO* mice. Auranofin increased eWAT OCR in wild-type mice compared to vehicle controls (Figure 7E) while we detected no drug effect on OCR in eWAT of *LepR KO* mice. Combined with gene expression and histology changes that implied less hepatic steatosis (Figure 2), these results argued auranofin causes primary impacts on eWAT to govern inter-organ responses that overcome the fatty acid demands of obesity.

The influence of leptin on sympathetic tone in eWAT (Wang et al., 2020; Zeng et al., 2015) raised the question of whether the effects of auranofin depend upon βAR signaling. Accordingly, we investigated the effects of auranofin on lipolysis in eWAT isolated from wild-type mice or beta-less mice, which lack all three βARs (Bachman et al., 2002). Auranofin alone significantly increased glycerol release from wild-type eWAT compared to controls (Figure 7F) but did not add to lipolysis responses in the presence of 10 μM isoproterenol, a non-selective βAR agonist. As expected, beta-less eWAT lacked functional responses to isoproterenol or auranofin treatments. Following the lipolysis studies, eWAT samples were subjected to immunoblotting to test activation of lipolysis (p-HSL) downstream of the βAR. p-HSL increased in wild-type eWAT exposed to isoproterenol, but no effects were observed in beta-less eWAT (Figure 7G). Interestingly, auranofin alone markedly increased p-HSL levels consistent with increased glycerol release compared to the vehicle control. To further understand the impact of auranofin on the leptin/βAR axis, we compared lipolytic responses in eWAT of obese wild-type and *LepR KO* mice and found auranofin increased sensitivity to βAR activation in wild-type eWAT (Figure 7H). At 1 μM isoproterenol, auranofin combined with βAR stimulation increased glycerol release compared to vehicle. In contrast, *LepR KO* eWAT only responded at the highest doses of isoproterenol (10 μM). Additionally, the complete absence of leptin rendered eWAT tissues from *ob/ob* mice unresponsive to isoproterenol (Figure S5J). Activation of βARs and liberation of FFA from WAT inhibit leptin secretion (Cammisotto et al., 2003; Ricci et al., 2005). Along these lines, ELISAs performed with conditioned media revealed auranofin decreased leptin secretion by wild-type eWAT, which was further suppressed in the presence of isoproterenol (Figure 7I), suggesting auranofin impinges upon secretion to lower bioavailable leptin in the serum. Leptin secretion from *LepR KO* eWAT explants remained high and unaffected by auranofin or isoproterenol. Together, these data demonstrate auranofin increases βAR sensitivity, thereby restoring lipolytic competence and regulation of leptin secretion.

Inflammation and macrophage abundance can de-regulate lipolytic responses by interfering with sympathetic neurons in eWAT of obese mice (Camell et al., 2017; Mowers et al., 2013; Valentine et al., 2022). Although auranofin reduced some markers of macrophage abundance in eWAT (Figure 3G), other features showed variable patterns, including indistinguishable Mac2 staining between control and drug treatments. (Figure 7J). We also noticed *LepR KO* displayed considerably lower Mac2 labeling than wild-type mice, likely attributed to the loss of leptin chemoattractant actions (Chen et al., 2021; Dib et al., 2014). This observation was confirmed by a secondary marker that showed fewer CD68+ macrophages in *LepR KO* compared to wild-type mice, suggesting any metabolic effects of auranofin on immune cells occur secondary to leptin lowering. Western blotting of eWAT demonstrated the leptin reduction performed by auranofin in wild-type mice was required to increase the marker

of sympathetic neuron content, tyrosine hydroxylase (Figure 7K), and form a platform for greater lipolytic competence.

DISCUSSION

Overall, our experiments identified an insulin sensitizer that acts on leptin secretion as a treatment for obesity and its comorbidities. Auranofin received FDA approval in 1985 for RA, an inflammatory condition often coupled with higher serum leptin levels (Baker et al., 2022) and co-morbidities of T2DM (Giles et al., 2018). Our findings align with the metabolic impacts of other anti-inflammatory RA drugs, which improve insulin sensitivity in retrospective analyses (Collotta et al., 2020; Ursini et al., 2018). However, leptin reduction does not occur during the management of RA (Novella-Navarro et al., 2022), which portrays our findings as new clinical endpoints of auranofin in frank obesity.

Auranofin spares the brain. Along these lines, auranofin levels in the brain after injections were only detected in nominal amounts (Walz et al., 1983). In humans, auranofin reduces macrophage accumulation and pro-inflammatory cytokine expression in the lipophilic, synovial membrane of RA patients (Handel et al., 1995; Yanni et al., 1994). Owing to its hydrophobicity, auranofin selectively accrues in the highly lipid-rich environment of WAT to diminish the activities of inflammatory cells and their cytokines. Further, in line with the capture of auranofin within fat tissues, we found enhanced insulin sensitivity underscored by augmented glucose disposal in eWAT and recruitment of metabolic pathways that burn carbohydrates and lipids. These observations suggest that the primary effects of auranofin occur on WAT.

As mechanisms of action, auranofin exerts pleiotropic effects. Auranofin can induce reactive oxygen species (Nakaya et al., 2011) but also dampen pro-inflammatory Nf-kB activities associated with poor WAT expandability (Jeon et al., 2000). Although extremely high levels of reactive oxygen species cause cellular damage, moderate production entrains a tolerable oxidative environment that enhances adipocyte differentiation (Han et al., 2016). Structurally, the gold contributes to the anti-inflammatory properties of auranofin, while the sulfur atom participates in redox reactions with selenium-containing proteins (Bak et al., 2018). Notably, auranofin increased genes encoding selenium-dependent glutathione catabolism enzymes in eWAT, whose expression contributes to adipocyte differentiation and forms barriers against free radical damage associated with obesity (Shan et al., 2022).

Despite durable correlations between inflammation and obesity in humans and mice, causal relationships between WAT inflammation and insulin resistance remain unclear. The historical failure of anti-inflammatory therapies (Goldfine et al., 2013; Goldfine et al., 2010; Ofei et al., 1996) for treating obesity further suggests alternate roles for immune cells that respond to overnutrition. Potent inflammatory responses can enable the organism to cope with metabolic stress and deliver signals essential for adipose tissue integrity and insulin sensitivity during HFD (Shimobayashi et al., 2018; Wernstedt Asterholm et al., 2014; Zhu et al., 2020). Moreover, single-cell studies expanded the diversity of WAT macrophages and redefined the suitability of surface markers, like CD11c and CD206, used to classify diet-induced inflammation and extrapolate pathological effects (Burl et al., 2018; Hildreth

et al., 2021; Hill et al., 2018). These factors may contribute to variable assignments of macrophage functions in obesity. In our study, obesity caused by genetic hyperleptinemia negated the metabolic effects of auranofin and macrophages appeared absent in eWAT. These combined observations suggest canonically defined eWAT inflammation may not be obligate for insulin resistance in obesity. Although our findings do not rule out the idea that anti-inflammatory monotherapies will be effective metabolic interventions, they argue strongly leptin lowering improves all the clinical phenotypes of obesity and T2DM.

Restoration of βAR sensitivity in WAT enables lipolysis and body composition changes beneficial for diseases such as obesity. We propose auranofin tempers leptin levels coupled with re-sensitized βAR regulation of lipolysis. While long considered an important component of thermogenesis (Collins et al., 2010; Himms-Hagen et al., 1994), neural inputs regulate βAR signaling and lipolysis in WAT, playing a critical role in serving the energy demands of the organism (Pirzgalska et al., 2017; Zeng et al., 2015). Interestingly, leptin elevates WAT innervation (Wang et al., 2020), catecholamine content in WAT, and activates lipolysis through βAR and p-HSL (Zeng et al., 2015). Newly discovered features of auranofin included increased tyrosine hydroxylase abundance, βAR sensitivity, and p-HSL activation in eWAT that coincided with upregulated fatty acid metabolic gene programs and OCR, which may sequester FFA from the liver in part to resolve steatosis. Auranofin may also influence innervation of the islet to re-establish glucose-stimulated insulin secretion in obese mice. Along these lines, implementation of modern 3D methods (Alvarsson et al., 2020) to map nerve contacts with β cells will critically define more far reaching effects of auranofin accumulation in WAT.

In obese humans, we showed reduced expression of *ADRB3* and *HSL/LIPE,* which encode crucial elements of catecholamine action, lipolysis, and directed control of leptin secretion (Cammisotto et al., 2003; Ricci et al., 2005; Valentine et al., 2022). Leptin levels remained high in *LepR KO* mice, and auranofin does not elevate expression of lipolytic genes nor increase TH abundance although the latter may require intact leptin signaling (Wang et al., 2020). Consequently, intact LEPR was also needed for auranofin to engage the βAR and reduce leptin secretion from eWAT. In parallel with improvement of eWAT metabolic fitness, our studies implicate auranofin exerts local effects and help explain why high circulating concentrations of leptin in obese animals have little effect on fat cell βAR sensitivity (Wang et al., 2005). Ultimately, our observations add to recent studies (Zhao et al., 2020; Zhao et al., 2019) and suggest the pharmacological reduction of leptin levels under obese conditions, through the use of auranofin, may offer largely weight agnostic effects but confers anti-diabetic properties associated with the ability to titrate down serum leptin concentrations and restore WAT lipolytic competence.

A strength of our study is that we performed experiments at auranofin doses near the human bioequivalent and showed auranofin improves the overall metabolic phenotype of obesity encompassing body weight, insulin sensitivity, normalization of serum leptin levels, and reduction of fatty liver. Our treatment regimen induced modest decreases in body weight but promoted locomotor activity derived from peripheral leptin functions. Leptin stimulates locomotor activity in obese mice, independent of food intake and body weight (Huo et al., 2009). Similarly, auranofin increased locomotor activity in mice with intact leptin signaling.

To translate our findings to persons living with obesity, it will be essential to use clinical studies and tracer methods to uncover how auranofin and leptin lowering impact activity and glucose disposal at physiologic and molecular levels.

Auranofin has been used to treat RA patients for years, so the human dosing and toxicological data are known. To date, fourteen clinical trials tested auranofin's clinical efficacy in cancer, HIV, and other infectious diseases (https://www.clinicaltrials.gov). Yet, none of the studies monitored glucose or other energy balance variables as outcomes. The scarcity of information related to metabolic hormones when individuals are on RA drugs stems from the fact that the persons also received other therapies in combination that interfere with blood sugar, including glucocorticoids and methotrexate. It is unclear how efficacious auranofin might be for persons with obesity and T2DM. Therefore, a controlled clinical study for auranofin with primary endpoints of glucose disposal will validate and support ongoing efforts to repurpose affordable drugs for treating obesity and its co-morbidities.

LIMITATIONS OF THE STUDY

The molecular mechanisms of auranofin remain unclear and no unifying theory has been proposed to our knowledge despite the numerous targets described. Considering *miR-30a* deletion can be reconciled by any one of the other five *miR-30* family members, we cannot exclude that auranofin activities intersect other microRNAs not covered in this study. Nonetheless, the thermogenic influences of *miR-30* (Hu et al., 2015; Koh et al., 2018) and lipolytic responses of auranofin require catecholamine sensitivity, which we speculate converges some of *miR-30a* and auranofin effects in WAT. Auranofin selectively augmented glucose uptake in WAT that dominated whole body glucose disposal rates, with differences likely accounted for by other tissues not measured in our study. These results were unexpected but seem to indicate beneficial effects of auranofin arise from accumulation in WAT. Likewise, intraperitoneal injections deliver auranofin readily into lipophilic tissues, while per orem administrations are less bioavailable (Gottlieb, 1983; Walz et al., 1983). Thus, identifying oral auranofin doses will be important efforts for future clinical trials in people living with obesity. Another limitation of our study is that the drug has not been tested in female mouse models of obesity and a complete lack of leptin causes infertility. However, we expect leptin lowering by auranofin spares fertility (Zhao et al., 2019). Lastly, we believe the anti-diabetic actions of leptin lowering are probably more relevant than the impact on WAT inflammation. In this regard, our study fills a fundamental gap in the literature by demonstrating how local leptin actions in WAT improve insulin sensitivity.

STAR METHODS

RESOURCE AVAILABILITY

Lead Contact—Further information and requests for resources should be directed to and will be fulfilled by the Lead Contact, Sean M. Hartig (hartig@bcm.edu).

Materials Availability—Unique resources (*miR-30a*$^{-/-}$ mice) generated during the study are available from the Lead Contact.

Data and code availability

- Source data for graphs can be found in Data S1. The RNA-seq data have been deposited in GEO (GSE202935) and are publicly available. The accession number is provided in the key resources table.
- This paper does not report original code.
- Any additional information required to reanalyze data reported in this paper is available from the lead contact.

EXPERIMENTAL MODEL AND SUBJECT DETAILS

Mice and housing conditions—All animal procedures were approved by the Institutional Animal Care and Use Committee of Baylor College of Medicine. All experiments were conducted using littermate-controlled male mice aged 6-8 weeks. All mice were housed in a barrier-specific pathogen-free animal facility with 12 h dark-light cycle and free access to water and food. C57BL/6J wild-type mice and FVB (control mice for beta-less experiments) mice were obtained from the BCM Center for Comparative Medicine. Mice were fed 60% high-fat diet (HFD; Bio-Serv) for 12 weeks before experiments. *Ubc-Cre;LepR*$^{lp/lp}$ (*LepR KO*) mice were generated previously (Cox et al., 2016). Male *LepR KO* mice were treated with 0.1 mg/g body weight tamoxifen by oral gavage (Cox et al., 2016) at 8 weeks of age to induce *LepR* gene deletion. Beta-less mice (*Adbr1, Adbr2, Adrb3* triple knockout) were bred in-house to generate 3-month-old mice for *ex vivo* studies. Mice were injected with auranofin (1, 5, 7.5, or 10 mg/kg body weight) or vehicle control (5% DMSO, 5% polyethylene glycol, 10% ethanol, PBS) three days per week for 4 weeks, followed by metabolic phenotyping. At the end of experiments, mice were euthanized by cervical dislocation while under isoflurane anesthesia. After euthanasia, tissues were collected, flash-frozen in liquid N_2, and stored at −80°C until use. All experiments adhered to ARRIVE Guidelines.

Human adipose tissue—Subcutaneous WAT RNA and plasma samples were obtained previously (Cifarelli et al., 2020) and applied the following inclusion criteria for each of the 2 groups: (a) metabolically healthy lean had BMI 18.5–24.9 kg/m^2, plasma TG concentration <150 mg/dL, fasting plasma glucose concentration <100 mg/dL, 2-hour OGTT plasma glucose concentration <140 mg/dL, HbA1c ≤5.6%, and IHTG content <4%; (b) metabolically unhealthy obese (MUO) had BMI 30–49.9 kg/m^2, prediabetes (fasting plasma glucose concentration ≥100 mg/dL, 2-hour OGTT plasma glucose concentration ≥140 mg/dL, and/or HbA1c ≥5.7%), and IHTG content ≥5%.

Generation of *miR-30a*$^{-/-}$ mice—*miR-30a*$^{-/-}$ mice were generated with the BCM Genetically Engineered Rodent Models Core. Single guide RNAs (sgRNA) flanked a 1 kb region on mouse chromosome 1 (mm10_dna range=chr1:23272064-23272543) that contains *miR-30a.* sgRNA sequences were designed to target the genomic sequences using upstream sgRNA, 5′-ACTCCCGCAGAGCACTTCTCAGG-3′ and downstream sgRNA, 5′-TCAAGGAGTAATTATCTTGTTGG-3′. To minimize the probability of off-target events, only sgRNAs predicted to have off-target sites with three mismatches or more were used to target Cas9 endonuclease activity to regions flanking the *miR-30a* gene. Two hundred

C57BL/6NJ pronuclear-stage zygotes were co-injected with 100 ng/μl Cas9 mRNA, 20 ng/μl sgRNA (each), and 100 ng/μl of ssODNs. Following microinjection, zygotes were transferred into pseudopregnant ICR recipient females at approximately 25–32 zygotes per recipient. Sanger sequencing and founder line genotyping from mouse genomic DNA confirmed the deletion. DNA extracted from mouse ear clips was used in PCR reactions with primers designed to detect the deleted alleles. Primer sequences (5'→3') that flanked the *miR-30a* locus for genotyping were: GCATCGAGGCTTTGCAGTTT and TGCACAGGAAGAACACTTCTGT.

The TaqMan Advanced miRNA cDNA Synthesis Kit (ThermoFisher, #A28007) was used to synthesize miRNA cDNA from 20 ng total RNA. To extend mature miRNAs, polyadenylation and adaptor sequence ligation of the 3' and 5' ends, respectively, occur before universal priming and reverse transcription. To address low-expressing targets, cDNA is amplified by primers that recognize sequences appended to both ends, effectively minimizing amplification bias. Next, the TaqMan Advanced miRNA Assays (ThermoFisher #A25576) were used to quantify relative gene expression. As recommended by the manufacturer, invariant RNA controls included *miR-423-3p, miR-451,* and *miR-423-5p.*

METHOD DETAILS

Connectivity Map (CMap) analysis—We previously performed RNA-seq analysis on total RNA from iWAT from mice expressing Adv-*miR-30a* or GFP control (Koh et al., 2018). Differentially expressed genes ($p<0.05$, Table S1) by Adv-*miR-30a* formed the gene signature to query the Broad Connectivity database (Lamb et al., 2006) which is comprised of transcriptional responses of human cells to different chemical and genetic perturbations (7,500 perturbagens). The result of a CMap query is a list of perturbagens rank-ordered by the similarity of differentially expressed gene sets to the query gene set. A positive score indicates similarity between a given perturbagen's signature and that of the query, while a negative score indicates that the two signatures are opposing (i.e., genes that are increased by treatment with the perturbagen are decreased in the query and vice versa). The CMap connectivity score is a standardized measure ranging from −100 to 100 and corresponds to the magnitude of similarity or dissimilarity.

Glucose and insulin tolerance tests—To determine glucose tolerance, mice were fasted 16 h, and glucose was administered 1.5 g/kg body weight by intraperitoneal injection. To determine insulin tolerance, mice were fasted four hours before i.p. insulin injection (1.5 U/kg (HFD) or 0.75 U/kg (normal chow) body weight). Blood glucose levels were measured by handheld glucometer. ELISA quantified serum hormone levels for overnight fasting insulin (Millipore #EZRMI-13K), fed leptin (Crystal Chem #90030), and soluble DPP4 (Thermo Fisher #EMDPP4). Mouse body composition was examined by MRI (Echo Medical Systems).

Hyperinsulinemic-euglycemic clamp studies—The hyperinsulinemic-euglycemic clamp studies were performed in unrestrained mice as previously described (Ding et al., 2021). Mice were catheterized in the right jugular vein and allowed to recover for 4–7 days. After overnight fasting, mice received a primed dose of [^{3}H]-glucose (10 μCi) and

then a constant rate intravenous infusion (0.1 μCi/min) of [^{3}H]-glucose using a syringe infusion pump for 90 min. Blood samples were collected for the determination of basal glucose production. After 90 min, mice were then primed with a bolus injection of insulin followed by a 2 h continuous insulin infusion. Simultaneously, 25% glucose was infused at an adjusted rate to maintain the blood glucose level at 100–140 mg/dl. Blood glucose concentration was determined every 10 min by glucometer. At the end of a 120-min period, blood was collected for the measurements of hepatic glucose production and peripheral glucose disposal rates. For tissue-specific uptake, we injected 2-deoxy-D-[1-^{14}C]-glucose (10 μCi) during the hyperinsulinemic-euglycemic clamp 45 min before the end of the clamp and collected blood samples at 5, 10, 15, 25, 35, and 45 min. At the end of the clamp, mouse tissues were harvested to evaluate glucose uptake. Glucose uptake in different tissues was calculated from plasma 2-[^{14}C]-deoxyglucose profile and tissue content of [^{14}C]-glucose-6 phosphate.

Indirect calorimetry—Mice were maintained on HFD and housed at room temperature in Comprehensive Lab Animal Monitoring System Home Cages (CLAMS-HC, Columbus Instruments). O_2 consumption, CO_2 emission, energy expenditure, food and water intake, and activity were measured for seven days (BCM Mouse Metabolic Phenotyping Core). Body weight was recorded, and body composition was examined by MRI prior to indirect calorimetry.

Immunoblotting—Tissue lysates were prepared in Tissue Protein Extraction Reagent (Thermo Fisher #78510) supplemented with Halt Protease and Phosphatase Inhibitor Cocktail (Thermo Fisher #78440). Immunoblotting was performed with lysates run on 4-12% Bis-Tris NuPage gels (Life Technologies #NP0321Box) and transferred onto Immobilon-P Transfer Membranes (Millipore #IPVH00010) followed by incubation with antibodies against p-AKT (Ser473; Cell Signaling #4060, RRID:AB_2315049), pan AKT (Cell Signaling #4691, RRID:AB_915783), adiponectin (GeneTex #GTX112777; RRID:AB_2885323), p-HSL (Ser563, Cell Signaling #4139, RRID:AB_2135495), total HSL (Cell Signaling #4107, RRID:AB_2296900), TH (Pel-Freez Biologicals #P40101-150, RRID:AB_2617184), beta actin (Sigma #A5441, RRID:AB_476744), HSP90 (GeneTex #GTX110089, RRID:AB_1950529), GAPDH (Cell Signaling #2118, RRID:AB_561053), and MAC2 (Novus #NBP1-43313, RRID:AB_10006681). Immunoreactive bands were visualized by chemiluminescence or the Odyssey Imaging System (Li-COR).

qPCR—Total RNA was extracted using the Direct-zol RNA MiniPrep kit (Zymo Research #R2051). cDNA was synthesized using qScript (QuantBio #95048-100). Relative mRNA expression was measured with SsoAdvanced Universal Probes Supermix reactions (Bio-Rad #175284) read out with a QuantStudio 3 real-time PCR system (Applied Biosystems). TATA-box binding protein (*Tbp)* was the invariant control. Roche Universal Probe Gene Expression Assays were used as previously described (Koh et al., 2018). Table S3 in the key Resources Table lists the primers and qPCR assays used in this study. TaqMan Gene Expression Assays (ThermoFisher #4331182) were used to detect *PPARG, PGC1a,* and *UCP1* expression in human adipocytes.

RNA-Seq—Snap-frozen tissues were sent to Novogene for RNA extraction and sequencing. Sample quality control was analyzed on Bioanalyzer 2100 (Agilent) followed by mRNA library prep using NEBNext Ultra II kit (non-stranded, poly-A selected; New England Biolabs #E7645S). The prepared libraries were sequenced using PE150 on the Illumina NovaSeq 6000, generating ~20 million paired reads/sample. Reads were mapped to the mouse reference genome mm 10 using STAR software. Differential expression analysis of auranofin versus vehicle treatment was performed using the DESeq2 R package. The resulting p values were adjusted using Benjamini and Hochberg's approach for controlling the false discovery rate. Gene set enrichment analysis was performed with the Molecular Signatures Database, and normalized enrichment scores were calculated for Hallmark gene sets.

In vitro experiments—SVF cells were isolated from mouse iWAT. Fat depots were digested in PBS containing collagenase I (1.5 U/ml; Roche #17100-017) and dispase II (2.4 U/ml; Sigma #D4693) supplemented with 10 mM $CaCl_2$ at 37°C for 40-45 min. The primary cells were filtered twice through 70 μm cell strainers and centrifuged at 700 rcf to collect the SVF. The SVF cell pellets were rinsed and plated. Adipocyte differentiation was induced by treating confluent cells in DMEM/F12 medium containing Glutamax (ThermoFisher #10565-018), 10% FBS, with 0.250 mM isobutylmethylxanthine (Sigma #13347), 1 mM rosiglitazone (Cayman Chemical Co. #71740), 1 mM dexamethasone (Tocris Biosciences #1126), 850 nM insulin (Sigma I5500), and 1 nM T3 (Sigma #T-074). Four days after induction, cells were switched to the maintenance medium containing 10% FBS, 1 mM rosiglitazone, 1 mM dexamethasone, 850 nM insulin, 1 nM T3. Experiments occurred 8-10 days after induction of differentiation. Subcutaneous human preadipocytes (Zen-Bio) were differentiated and transfected with microRNA mimics as described (Koh et al., 2016).

Microscopy and histology—Mitochondria were labeled using MitoTracker CMX-ROS (ThermoFisher #M7512). Live cells were pulsed with 500 nM MitoTracker for 15 min. Mitochondrial labeling was followed by cell fixation in 4% paraformaldehyde. Ammonium chloride was used to quench autofluorescence derived from residual paraformaldehyde. Fixed cells were incubated with guinea pig anti-perilipin 1 (Progen #GP-29; RRID:AB_2892611) primary antibody at room temperature for 2 h, then washed in 1x PBS containing 0.2% Triton X-100 (PBS-T) three times (5 min/wash), followed by incubation with Alexa Fluor 647-conjugated donkey anti-guinea pig IgG (Jackson ImmunoResearch Labs #706=605-148; RRID:AB_2340476). DAPI (Sigma #D8417) and LipidTOX (Life Technologies #H34475) were used for nuclei and lipid droplet labeling, respectively. Imaging was performed with the DeltaVision Core Image Restoration Microscope (GE Healthcare). Formalin-fixed, paraffin-embedded adipose and liver tissue sections were stained with hematoxylin and eosin (H/E) and Oil Red O stains, respectively, by the BCM Human Tissue Acquisition and Pathology Core. Four 20x fields of view per tissue were imaged using a Nikon Ci-L Brightfield microscope. Fiji software quantified adipocyte morphometry in histological sections of WAT (Galarraga et al., 2012) and immunofluorescence intensities.

For immunofluorescence (IF) staining of WAT, the deparaffinized sections were permeabilized with PBS-Tween (PBS-T) for 10 min followed by incubation with sodium citrate buffer at 95°C for 30 min for antigen retrieval. After being blocked in 5% bovine serum albumin, the sections were stained with primary antibodies at 4°C overnight and then washed with PBS-T three times (5 min/wash). The sections were then incubated with secondary antibodies at room temperature for 1 h. After washing with PBS-T three times, the sections were mounted for imaging under the Leica TCS SP5 Confocal Laser Scanning Microscope. The primary antibodies used were Mac2 (eBioscience #13-5301-82, RRID:AB_837113) and CD68 (Invitrogen #MA5-13324, RRID:AB_10987212). The secondary antibodies used were Alexa Fluor 488–conjugated donkey anti-mouse IgG and Alexa Fluor 647–conjugated donkey anti-rat IgG (Jackson ImmunoResearch Laboratories #715-545-151, RRID:AB_2341099; #712-606-153, RRID:AB_2340696).

IF staining of the hypothalamus was adapted from a previous study (Lee et al., 2016). After treatments, the brain was fixed with 4% paraformaldehyde (PFA) through cardiac perfusion. Following overnight fixation in 4% PFA, tissues were incubated sequentially with 20% sucrose and 30% sucrose for 2 d and frozen in Tissue-Tek OCT compound (Sakura Finetek #4583) in dry ice. A total of 48 sections (30 μm/section), including the whole arcuate nucleus (ARC), ventromedial hypothalamus (VMH) and dorsomedial hypothalamus (DMH) from each mouse, were collected using a cryostat (Leica). The floating sections were washed with PBS for 5 min three times at room temperature and then sequentially incubated with 0.3% H_2O_2-1% NaOH for 20 min, 0.3% glycine for 10 min, and 0.03% sodium dodecyl sulfate for 10 min. Following 1 h incubation with blocking buffer (3% normal goat serum, 0.3% Triton X-100, 0.02% NaN_3 in PBS), the sections were incubated with p-STAT3 Y705 antibody (1:2,000 in blocking buffer; Cell Signaling #9145, RRID_AB:2491009) for 2 d at 4°C. After washing for 5 min 0.05% Tween 20 in PBS three times, the sections were incubated with fluorescein isothiocyanate (FITC)-conjugated goat anti-rabbit IgG (ThermoFisher #A-11034, RRID:AB_2576217) for 1 h at room temperature. After three additional washes, the sections were placed on glass slides with coverslips and subjected to image analysis. Images from the whole hypothalamic area of each section were acquired with a Zeiss Axio imager M2M microscope using a 10x objective. Each whole hypothalamic image was stitched from ~24 individual images. The p-STAT3 fluorescence intensities were blindly analyzed using Fiji software and the embedded image analysis methods.

Flow cytometry—SVF cells were isolated from eWAT following digestion with collagenase type I (Worthington Biochemical Corporation). Cells were stained with Fc receptor blockade and antibodies to immune cell markers CD45 (Thermo Fisher #17-0451-82; RRID:AB_469392), F4/80 (Thermo Fisher #45-4801-82, RRID:AB_914345), CD11c (Thermo Fisher #12-0114-82, RRID:AB_465552), and CD206 (Bio-Rad Laboratories #MCA2235F, RRID:AB_324594) or respective isotype controls. Data were collected with an LSRII cytometer (BD Biosciences) and analyzed using Kaluza software (Beckman Coulter, Indianapolis, IN). Gating was performed on viable CD45+ cells, from which total macrophages were identified as F4/80+ high. Macrophages were classified as $CD11c^+/CD206^-$ “M1-like” macrophages and $CD206^+/CD11c^-$ “M2-like” macrophages.

Data were presented as cell numbers per gram adipose tissue calculated using counting beads (Biolegend #424902) or as percentages of total macrophages and SVF.

Mass spectrometry—We analyzed auranofin biodistribution with the NMR and Drug Metabolism Core at Baylor College of Medicine using previously established protocols (York et al., 2017). Briefly, plasma and tissue extracts were homogenized in ice-cold MeOH solutions. After vortexing and centrifugation (15 min at 15,000 × g), each supernatant was transferred to an autosampler vial, and 5.0 μl was injected into a system combining ultra-high performance liquid chromatography and quadrupole time of flight mass spectrometry for analysis. The concentration of auranofin was calculated based on standard curves in the corresponding matrices. The linear trapezoidal rule was used for area under the curve calculations.

Proteomics—Protein lysates were prepared by the BCM Antibody-Based Proteomics Core for reverse phase protein array assays. The Aushon 2470 Arrayer (Aushon BioSystems) with a 40 pin (185 μm) configuration was used to spot lysates onto nitrocellulose-coated slides (Grace Bio-Labs). The slides were probed with 220 antibodies against total and phospho-proteins using an automated slide stainer (Dako). Primary antibody binding was detected using a biotinylated secondary antibody followed by streptavidin-conjugated IRDye 680 fluorophore (LI-COR). Fluorescent-labeled slides were scanned on a GenePix AL4200 and the images were analyzed with GenePix Pro 7.0 (Molecular Devices). Background-subtracted total fluorescence intensities of each spot were normalized for variation in total protein (Sypro Ruby) and nonspecific labeling. For adipokine analysis, tissue lysates from four samples were pooled (125 μg/sample) and incubated with membranes from the Proteome Profiler Mouse Adipokine Array Kit (R&D Systems #ARY013) according to the manufacturer's instructions.

Ex vivo lipolysis—Fat pads were excised and cut into ~50 mg pieces in PBS on ice. At least two tissue pieces per mouse were allocated to each treatment group. Each tissue was placed in a well of a 24-well plate containing 0.5 ml Krebs buffer and incubated for 1 h at 37°C, 5% CO_2. Media was replaced with fresh Krebs buffer containing 100 nM auranofin or vehicle (DMSO) +/− 10 μM isoproterenol. After a 2 h incubation at 37°C, 5% CO_2, tissues were snap-frozen in liquid N_2 and media snap-frozen on dry ice. Glycerol was measured by colorimetric assay (Sigma #MAK117).

Seahorse assays—Respiration was measured in cultured adipocytes using an XF24 analyzer (Agilent). SVF cells were plated into V7-PS plates and grown to confluence. Cells were differentiated for 8-10 days before treatment with auranofin (1000 nM) or vehicle (DMSO) overnight. For the assay, media was replaced with assay media: 37 °C unbuffered DMEM containing 4.5 g/L glucose, sodium pyruvate (1 mmol/L), and L-glutamine (2 mmol/L). Measurements were made at 37 °C using 2-2-2 intervals. Basal respiration was defined before sequential addition of oligomycin, FCCP, rotenone, and antimycin A.

To measure metabolic activities ex vivo, eWAT was dissected, cut into small pieces (5 mg), and washed in assay media. One tissue piece was placed in the center of each XF24 Islet Capture Microplate well and covered with customized screens. Upon positioning the

screen, 500 μl of assay media containing either DMSO (vehicle) or 100 ng/ml auranofin was immediately added. Oxygen consumption and extracellular acidification rates were collected for at least 30 min.

QUANTIFICATION AND STATISTICAL ANALYSIS

The statistical details of experiments can be found in the figure legends. All data are presented as mean ± SEM, unless otherwise specified. All statistical analyses were conducted in Prism 9 (GraphPad). We used unpaired one- and two-tailed t-tests and one-way and two-way ANOVAs to compare means where appropriate. Mann-Whitney tests were used to compare adipocyte size. Embedded ANCOVA tools in CalR were used to determine significant changes in energy expenditure measurements collected from CLAMS cages. No statistical method was used to predetermine sample size. Our primary threshold for statistical significance was $p<0.05$. Unblinded analysis of histology and immunohistochemistry was performed by the investigators.

Supplementary Material

Refer to Web version on PubMed Central for supplementary material.

ACKNOWLEDGEMENTS

We thank Robb Moses, Tony Means and Mark Herman of Baylor College of Medicine for critical feedback. This work was funded by American Diabetes Association #1-18-IBS-105 (S.M.H.) and NIH R01DK114356 (S.M.H.), R01DK126042 (S.M.H.), R01DK109001 (K.S.), R01AG065197 (H.W.), and R01DK121348 (H.W.). This study was also funded (in part) by the BCM Bridge to Independence Program (A.R.C). The Reverse Phase Protein Array Core is supported by CPRIT RP170005, NCI Cancer Center Support Grant P30CA125123, and intramural funds from the Dan L. Duncan Cancer Center. Other BCM core services received support from NCI P30CA125123: Genetically Engineered Rodent Models, Human Tissue Acquisition and Pathology, and Integrated Microscopy.

INCLUSION AND DIVERSITY

We support inclusive, diverse, and equitable conduct of research.

REFERENCES

Afshin A, Forouzanfar MH, Reitsma MB, Sur P, Estep K, Lee A, Marczak L, Mokdad AH, Moradi-Lakeh M, Naghavi M, et al. (2017). Health effects of overweight and obesity in 195 countries over 25 years. N Engl J Med 377, 13–27. [PubMed: 28604169]

Alvarsson A, Jimenez-Gonzalez M, Li R, Rosselot C, Tzavaras N, Wu Z, Stewart AF, Garcia-Ocaña A, and Stanley SA (2020). A 3D atlas of the dynamic and regional variation of pancreatic innervation in diabetes. Sci Adv 6.

Bachman ES, Dhillon H, Zhang CY, Cinti S, Bianco AC, Kobilka BK, and Lowell BB (2002). betaAR signaling required for diet-induced thermogenesis and obesity resistance. Science 297, 843–845. [PubMed: 12161655]

Bak DW, Gao J, Wang C, and Weerapana E (2018). A quantitative chemoproteomic platform to monitor selenocysteine reactivity within a complex proteome. Cell Chem Biol 25, 1157–1167.e1154. [PubMed: 29983274]

Baker JF, England BR, George MD, Wysham K, Johnson T, Kunkel G, Sauer B, Hamilton BC, Hunter CD, Duryee MJ, et al. (2022). Elevations in adipocytokines and mortality in rheumatoid arthritis. Rheumatology (Oxford). *in press,* Mar 23.

Burl RB, Ramseyer VD, Rondini EA, Pique-Regi R, Lee YH, and Granneman JG (2018). Deconstructing adipogenesis induced by β3-adrenergic receptor activation with single-cell expression profiling. Cell Metab 28, 300–309.e304. [PubMed: 29937373]

Camell CD, Sander J, Spadaro O, Lee A, Nguyen KY, Wing A, Goldberg EL, Youm YH, Brown CW, Elsworth J, et al. (2017). Inflammasome-driven catecholamine catabolism in macrophages blunts lipolysis during ageing. Nature 550, 119–123. [PubMed: 28953873]

Cammisotto PG, Gélinas Y, Deshaies Y, and Bukowiecki LJ (2003). Regulation of leptin secretion from white adipocytes by free fatty acids. Am J Physiol Endocrinol Metab 285, E521–526. [PubMed: 12736159]

Chen KE, Lainez NM, and Coss D (2021). Sex differences in macrophage responses to obesity-mediated changes determine migratory and inflammatory traits. J Immunol 206, 141–153. [PubMed: 33268480]

Cifarelli V, Beeman SC, Smith GI, Yoshino J, Morozov D, Beals JW, Kayser BD, Watrous JD, Jain M, Patterson BW, et al. (2020). Decreased adipose tissue oxygenation associates with insulin resistance in individuals with obesity. J Clin Invest 130, 6688–6699. [PubMed: 33164985]

Collins S, Yehuda-Shnaidman E, and Wang H (2010). Positive and negative control of Ucp1 gene transcription and the role of β-adrenergic signaling networks. Int J Obes (Lond) 34 Suppl 1, S28–33. [PubMed: 20935662]

Collotta D, Hull W, Mastrocola R, Chiazza F, Cento AS, Murphy C, Verta R, Alves GF, Gaudioso G, Fava F, et al. (2020). Baricitinib counteracts metaflammation, thus protecting against diet-induced metabolic abnormalities in mice. Mol Metab 39, 101009. [PubMed: 32413585]

Cox AR, Lam CJ, Rankin MM, King KA, Chen P, Martinez R, Li C, and Kushner JA (2016). Extreme obesity induces massive beta cell expansion in mice through self-renewal and does not alter the beta cell lineage. Diabetologia 59, 1231–1241. [PubMed: 27003683]

Dib LH, Ortega MT, Fleming SD, Chapes SK, and Melgarejo T (2014). Bone marrow leptin signaling mediates obesity-associated adipose tissue inflammation in male mice. Endocrinology 155, 40–46. [PubMed: 24169547]

Ding G, Li X, Hou X, Zhou W, Gong Y, Liu F, He Y, Song J, Wang J, Basil P, et al. (2021). REV-ERB in GABAergic neurons controls diurnal hepatic insulin sensitivity. Nature 592, 763–767. [PubMed: 33762728]

Fiskus W, Saba N, Shen M, Ghias M, Liu J, Gupta SD, Chauhan L, Rao R, Gunewardena S, Schorno K, et al. (2014). Auranofin induces lethal oxidative and endoplasmic reticulum stress and exerts potent preclinical activity against chronic lymphocytic leukemia. Cancer Res 74, 2520–2532. [PubMed: 24599128]

Galarraga M, Campión J, Muñoz-Barrutia A, Boqué N, Moreno H, Martínez JA, Milagro F, and Ortiz-de-Solórzano C (2012). Adiposoft: automated software for the analysis of white adipose tissue cellularity in histological sections. J Lipid Res 53, 2791–2796. [PubMed: 22993232]

Giles JT, Ferrante AW, Broderick R, Zartoshti A, Rose J, Downer K, Zhang HZ, and Winchester RJ (2018). Adipose tissue macrophages in rheumatoid arthritis: prevalence, disease-related indicators, and associations with cardiometabolic risk factors. Arthritis Care Res 70, 175–184.

Goldfine AB, Conlin PR, Halperin F, Koska J, Permana P, Schwenke D, Shoelson SE, and Reaven PD (2013). A randomised trial of salsalate for insulin resistance and cardiovascular risk factors in persons with abnormal glucose tolerance. Diabetologia 56, 714–723. [PubMed: 23370525]

Goldfine AB, Fonseca V, Jablonski KA, Pyle L, Staten MA, and Shoelson SE (2010). The effects of salsalate on glycemic control in patients with type 2 diabetes: a randomized trial. Ann Intern Med 152, 346–357. [PubMed: 20231565]

Gottlieb NL (1983). Comparison of the kinetics of parenteral and oral gold. Scand J Rheumatol Suppl 51, 10–14. [PubMed: 6426043]

Gottlieb NL, Smith PM, and Smith EM (1972). Tissue gold concentration in a rheumatoid arthritic receiving chrysotherapy. Arthritis Rheum 15, 16–22. [PubMed: 5059639]

Han YH, Buffolo M, Pires KM, Pei S, Scherer PE, and Boudina S (2016). Adipocyte-specific deletion of manganese superoxide dismutase protects from diet-induced obesity through increased mitochondrial uncoupling and biogenesis. Diabetes 65, 2639–2651. [PubMed: 27284109]

Handel ML, McMorrow LB, and Gravallese EM (1995). Nuclear factor-kappa B in rheumatoid synovium. localization of p50 and p65. Arthritis Rheum 38, 1762–1770. [PubMed: 8849348]

Hildreth AD, Ma F, Wong YY, Sun R, Pellegrini M, and O'Sullivan TE (2021). Single-cell sequencing of human white adipose tissue identifies new cell states in health and obesity. Nat Immunol 22, 639–653. [PubMed: 33907320]

Hill DA, Lim HW, Kim YH, Ho WY, Foong YH, Nelson VL, Nguyen HCB, Chegireddy K, Kim J, Habertheuer A, et al. (2018). Distinct macrophage populations direct inflammatory versus physiological changes in adipose tissue. Proc Natl Acad Sci U S A 115, E5096–e5105. [PubMed: 29760084]

Himms-Hagen J, Cui J, Danforth E Jr., Taatjes DJ, Lang SS, Waters BL, and Claus TH (1994). Effect of CL-316,243, a thermogenic beta 3-agonist, on energy balance and brown and white adipose tissues in rats. Am J Physiol 266, R1371–1382. [PubMed: 7910436]

Hu F, Wang M, Xiao T, Yin B, He L, Meng W, Dong M, and Liu F (2015). miR-30 promotes thermogenesis and the development of beige fat by targeting RIP140. Diabetes 64, 2056–2068. [PubMed: 25576051]

Huang W, Dedousis N, Bhatt BA, and O'Doherty RM (2004). Impaired activation of phosphatidylinositol 3-kinase by leptin is a novel mechanism of hepatic leptin resistance in diet-induced obesity. J Biol Chem 279, 21695–21700. [PubMed: 14993225]

Huo L, Gamber K, Greeley S, Silva J, Huntoon N, Leng XH, and Bjørbaek C (2009). Leptin-dependent control of glucose balance and locomotor activity by POMC neurons. Cell Metab 9, 537–547. [PubMed: 19490908]

Isoda K, Young JL, Zirlik A, MacFarlane LA, Tsuboi N, Gerdes N, Schönbeck U, and Libby P (2006). Metformin inhibits proinflammatory responses and nuclear factor-kappaB in human vascular wall cells. Arterioscler Thromb Vasc Biol 26, 611–617. [PubMed: 16385087]

Jeffery E, Wing A, Holtrup B, Sebo Z, Kaplan JL, Saavedra-Pena R, Church CD, Colman L, Berry R, and Rodeheffer MS (2016). The adipose tissue microenvironment regulates depot-specific adipogenesis in obesity. Cell Metab 24, 142–150. [PubMed: 27320063]

Jeon KI, Jeong JY, and Jue DM (2000). Thiol-reactive metal compounds inhibit NF-kappa B activation by blocking I kappa B kinase. J Immunol 164, 5981–5989. [PubMed: 10820281]

Klein S, Gastaldelli A, Yki-Järvinen H, and Scherer PE (2022). Why does obesity cause diabetes? Cell Metab 34, 11–20. [PubMed: 34986330]

Knight ZA, Gonzalez B, Feldman ME, Zunder ER, Goldenberg DD, Williams O, Loewith R, Stokoe D, Balla A, Toth B, et al. (2006). A pharmacological map of the PI3-K family defines a role for p110alpha in insulin signaling. Cell 125, 733–747. [PubMed: 16647110]

Koh EH, Chen Y, Bader DA, Hamilton MP, He B, York B, Kajimura S, McGuire SE, and Hartig SM (2016). Mitochondrial activity in human white adipocytes is regulated by the ubiquitin carrier protein 9/microRNA-30a axis. J Biol Chem 291, 24747–24755. [PubMed: 27758866]

Koh EH, Chernis N, Saha PK, Xiao L, Bader DA, Zhu B, Rajapakshe K, Hamilton MP, Liu X, Perera D, et al. (2018). miR-30a remodels subcutaneous adipose tissue inflammation to improve insulin sensitivity in obesity. Diabetes 67, 2541–2553. [PubMed: 30002134]

Lamb J, Crawford ED, Peck D, Modell JW, Blat IC, Wrobel MJ, Lerner J, Brunet JP, Subramanian A, Ross KN, et al. (2006). The Connectivity Map: using gene-expression signatures to connect small molecules, genes, and disease. Science 313, 1929–1935. [PubMed: 17008526]

Lee J, Liu J, Feng X, Salazar Hernández MA, Mucka P, Ibi D, Choi JW, and Ozcan U (2016). Withaferin A is a leptin sensitizer with strong antidiabetic properties in mice. Nat Med 22, 1023–1032. [PubMed: 27479085]

Lu M, Sarruf DA, Talukdar S, Sharma S, Li P, Bandyopadhyay G, Nalbandian S, Fan W, Gayen JR, Mahata SK, et al. (2011). Brain PPAR-γ promotes obesity and is required for the insulin-sensitizing effect of thiazolidinediones. Nat Med 17, 618–622. [PubMed: 21532596]

Lumeng CN, Bodzin JL, and Saltiel AR (2007). Obesity induces a phenotypic switch in adipose tissue macrophage polarization. J Clin Invest 117, 175–184. [PubMed: 17200717]

Mowers J, Uhm M, Reilly SM, Simon J, Leto D, Chiang SH, Chang L, and Saltiel AR (2013). Inflammation produces catecholamine resistance in obesity via activation of PDE3B by the protein kinases IKKε and TBK1. Elife 2, e01119. [PubMed: 24368730]

Mulvihill EE, and Drucker DJ (2014). Pharmacology, physiology, and mechanisms of action of dipeptidyl peptidase-4 inhibitors. Endocr Rev 35, 992–1019. [PubMed: 25216328]

Nakaya A, Sagawa M, Muto A, Uchida H, Ikeda Y, and Kizaki M (2011). The gold compound auranofin induces apoptosis of human multiple myeloma cells through both downregulation of STAT3 and inhibition of NF-κB activity. Leuk Res 35, 243–249. [PubMed: 20542334]

Novella-Navarro M, Genre F, Hernández-Breijo B, Remuzgo-Martínez S, Martínez-Feito A, Peiteado D, Monjo I, González-Gay M, Plasencia-Rodríguez C, and Balsa A (2022). Obesity and response to biological therapy in rheumatoid arthritis: the role of body mass index and adipose tissue cytokines. Clin Exp Rheumatol. *in press,* Jan 12.

Ofei F, Hurel S, Newkirk J, Sopwith M, and Taylor R (1996). Effects of an engineered human anti-TNF-alpha antibody (CDP571) on insulin sensitivity and glycemic control in patients with NIDDM. Diabetes 45, 881–885. [PubMed: 8666137]

Pirzgalska RM, Seixas E, Seidman JS, Link VM, Sánchez NM, Mahú I, Mendes R, Gres V, Kubasova N, Morris I, et al. (2017). Sympathetic neuron-associated macrophages contribute to obesity by importing and metabolizing norepinephrine. Nat Med 23, 1309–1318. [PubMed: 29035364]

Reilly SM, Chiang SH, Decker SJ, Chang L, Uhm M, Larsen MJ, Rubin JR, Mowers J, White NM, Hochberg I, et al. (2013). An inhibitor of the protein kinases TBK1 and IKK-ε improves obesity-related metabolic dysfunctions in mice. Nat Med 19, 313–321. [PubMed: 23396211]

Ricci MR, Lee MJ, Russell CD, Wang Y, Sullivan S, Schneider SH, Brolin RE, and Fried SK (2005). Isoproterenol decreases leptin release from rat and human adipose tissue through posttranscriptional mechanisms. Am J Physiol Endocrinol Metab 288, E798–804. [PubMed: 15585586]

Rohm TV, Meier DT, Olefsky JM, and Donath MY (2022). Inflammation in obesity, diabetes, and related disorders. Immunity 55, 31–55. [PubMed: 35021057]

Sakers A, De Siqueira MK, Seale P, and Villanueva CJ (2022). Adipose-tissue plasticity in health and disease. Cell 185, 419–446. [PubMed: 35120662]

Samms RJ, Christe ME, Collins KA, Pirro V, Droz BA, Holland AK, Friedrich JL, Wojnicki S, Konkol DL, Cosgrove R, et al. (2021). GIPR agonism mediates weight-independent insulin sensitization by tirzepatide in obese mice. J Clin Invest 131, e146353. [PubMed: 34003802]

Shan B, Barker CS, Shao M, Zhang Q, Gupta RK, and Wu Y (2022). Multilayered omics reveal sex- and depot-dependent adipose progenitor cell heterogeneity. Cell Metab 34, 783–799.e787. [PubMed: 35447091]

Shimobayashi M, Albert V, Woelnerhanssen B, Frei IC, Weissenberger D, Meyer-Gerspach AC, Clement N, Moes S, Colombi M, Meier JA, et al. (2018). Insulin resistance causes inflammation in adipose tissue. J Clin Invest 128, 1538–1550. [PubMed: 29528335]

Soccio RE, Chen ER, and Lazar MA (2014). Thiazolidinediones and the promise of insulin sensitization in type 2 diabetes. Cell Metab 20, 573–591. [PubMed: 25242225]

Tan S, Ng Y, and James DE (2011). Next-generation Akt inhibitors provide greater specificity: effects on glucose metabolism in adipocytes. Biochem J 435, 539–544. [PubMed: 21348862]

Ursini F, Russo E, Ruscitti P, Giacomelli R, and De Sarro G (2018). The effect of non-TNF-targeted biologics and small molecules on insulin resistance in inflammatory arthritis. Autoimmun Rev 17, 399–404. [PubMed: 29452240]

Valentine JM, Ahmadian M, Keinan O, Abu-Odeh M, Zhao P, Zhou X, Keller MP, Gao H, Yu RT, Liddle C, et al. (2022). β3-Adrenergic receptor downregulation leads to adipocyte catecholamine resistance in obesity. J Clin Invest 132, e153357. [PubMed: 34847077]

Vernon-Roberts B, Doré JL, Jessop JD, and Henderson WJ (1976). Selective concentration and localization of gold in macrophages of synovial and other tissues during and after chrysotherapy in rheumatoid patients. Ann Rheum Dis 35, 477–486. [PubMed: 1087551]

Walz DT, DiMartino MJ, Griswold DE, Intoccia AP, and Flanagan TL (1983). Biologic actions and pharmacokinetic studies of auranofin. Am J Med 75, 90–108.

Wang MY, Orci L, Ravazzola M, and Unger RH (2005). Fat storage in adipocytes requires inactivation of leptin's paracrine activity: implications for treatment of human obesity. Proc Natl Acad Sci U S A 102, 18011–18016. [PubMed: 16326804]

Wang P, Loh KH, Wu M, Morgan DA, Schneeberger M, Yu X, Chi J, Kosse C, Kim D, Rahmouni K, et al. (2020). A leptin-BDNF pathway regulating sympathetic innervation of adipose tissue. Nature 583, 839–844. [PubMed: 32699414]

Weisberg SP, McCann D, Desai M, Rosenbaum M, Leibel RL, and Ferrante AW Jr. (2003). Obesity is associated with macrophage accumulation in adipose tissue. J Clin Invest 112, 1796–1808. [PubMed: 14679176]

Wentworth JM, Zhang JG, Bandala-Sanchez E, Naselli G, Liu R, Ritchie M, Smyth GK, O'Brien PE, and Harrison LC (2017). Interferon-gamma released from omental adipose tissue of insulin-resistant humans alters adipocyte phenotype and impairs response to insulin and adiponectin release. Int J Obes (Lond) 41, 1782–1789. [PubMed: 28769120]

Wernstedt Asterholm I, Tao C, Morley TS, Wang QA, Delgado-Lopez F, Wang ZV, and Scherer PE (2014). Adipocyte inflammation is essential for healthy adipose tissue expansion and remodeling. Cell Metab 20, 103–118. [PubMed: 24930973]

Wittman M, Carboni J, Attar R, Balasubramanian B, Balimane P, Brassil P, Beaulieu F, Chang C, Clarke W, Dell J, et al. (2005). Discovery of a (1H-benzoimidazol-2-yl)-1H-pyridin-2-one (BMS-536924) inhibitor of insulin-like growth factor I receptor kinase with in vivo antitumor activity. J Med Chem 48, 5639–5643. [PubMed: 16134929]

Yanni G, Nabil M, Farahat MR, Poston RN, and Panayi GS (1994). Intramuscular gold decreases cytokine expression and macrophage numbers in the rheumatoid synovial membrane. Ann Rheum Dis 53, 315–322. [PubMed: 8017985]

York B, Li F, Lin F, Marcelo KL, Mao J, Dean A, Gonzales N, Gooden D, Maity S, Coarfa C, et al. (2017). Pharmacological inhibition of CaMKK2 with the selective antagonist STO-609 regresses NAFLD. Sci Rep 7, 11793. [PubMed: 28924233]

Zeng W, Pirzgalska RM, Pereira MM, Kubasova N, Barateiro A, Seixas E, Lu YH, Kozlova A, Voss H, Martins GG, et al. (2015). Sympathetic neuro-adipose connections mediate leptin-driven lipolysis. Cell 163, 84–94. [PubMed: 26406372]

Zhao S, Li N, Zhu Y, Straub L, Zhang Z, Wang MY, Zhu Q, Kusminski CM, Elmquist JK, and Scherer PE (2020). Partial leptin deficiency confers resistance to diet-induced obesity in mice. Mol Metab 37, 100995. [PubMed: 32289482]

Zhao S, Zhu Y, Schultz RD, Li N, He Z, Zhang Z, Caron A, Zhu Q, Sun K, Xiong W, et al. (2019). Partial leptin reduction as an insulin sensitization and weight loss strategy. Cell Metab 30, 706–719.e706. [PubMed: 31495688]

Zhu Q, An YA, Kim M, Zhang Z, Zhao S, Zhu Y, Asterholm IW, Kusminski CM, and Scherer PE (2020). Suppressing adipocyte inflammation promotes insulin resistance in mice. Mol Metab 39, 101010. [PubMed: 32408016]

HIGHLIGHTS

- The rheumatoid arthritis drug auranofin improves insulin sensitivity in obese mice
- Auranofin accumulation in epididymal white fat drives whole-body glucose disposal
- Metabolic benefits of auranofin require an intact leptin axis
- Auranofin couples lipolytic competence to inhibition of leptin secretion

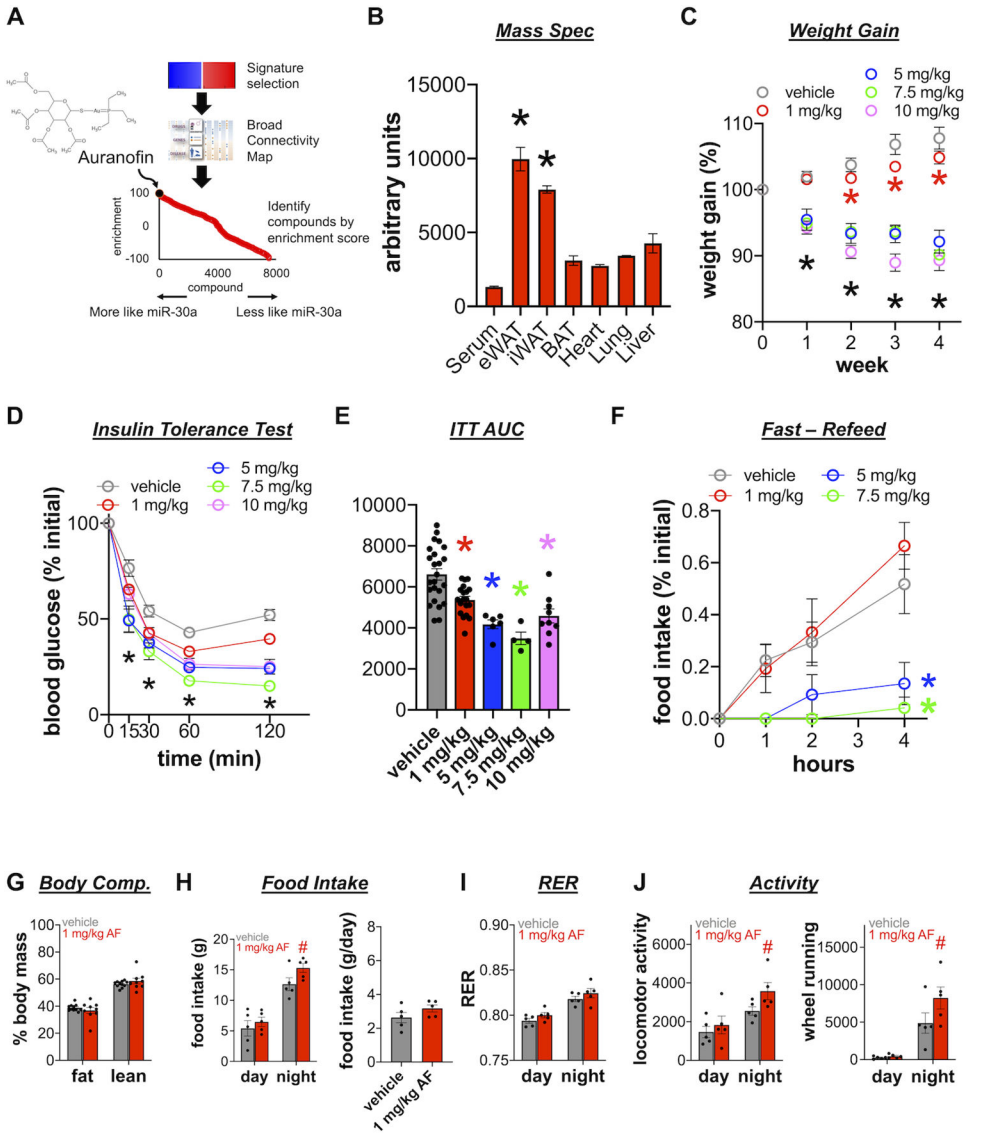

Figure 1. The RA drug auranofin and *miR-30a* exhibit similar activities.

(A) The Broad Connectivity Map identified auranofin regulates gene expression in a similar way as *miR-30a* expression in iWAT. **(B)** Diet-induced obese mice injected with auranofin i.p. (10 mg/kg) and sacrificed 24 h later for mass spectrometry analysis of tissue distribution. Wild-type mice fed high-fat diet (HFD) for 12 weeks i.p. injected with auranofin (1, 5, 7.5, 10 mg/kg) or vehicle for 4 weeks. **(C)** Weight gain for vehicle n=24, 1 mg/kg n=29, 5 mg/kg n=6, 7.5 mg/kg n=4, 10 mg/kg n=10. **(D)** ITT with corresponding **(E)** area under the curve measurements. **(F)** Food intake measured in mice fasted 16 h and re-fed after auranofin injection (n=4-5/group). **(G)** Body composition (n=9-14/group). Mice were individually housed and monitored in CLAMS cages for 7 days (1 mg/kg, n=5/group). Averaged data during dark/light periods for **(H)** food intake, **(I)** RER, and **(J)** activity.

All data are mean ± SEM. *p<0.05, #p<0.10 by one-way ANOVA with Tukey's multiple comparison test (**B**; **E**), mixed-effects analysis with Tukey's multiple comparisons test (**C**, black asterisks are week 1 vehicle vs 5, 7.5, 10 mg/kg and red asterisks are weeks 2-4

vehicle vs 1 mg/kg; **D**, ITT% vs vehicle; **F**, hours 2-4 vehicle or 1 mg/kg vs 5 and 10 mg/kg), two-way ANOVA with Tukey's multiple comparisons test (**G**; day/night food intake, **H**), and ANCOVA with lean mass as a covariate (**I**; **J**)

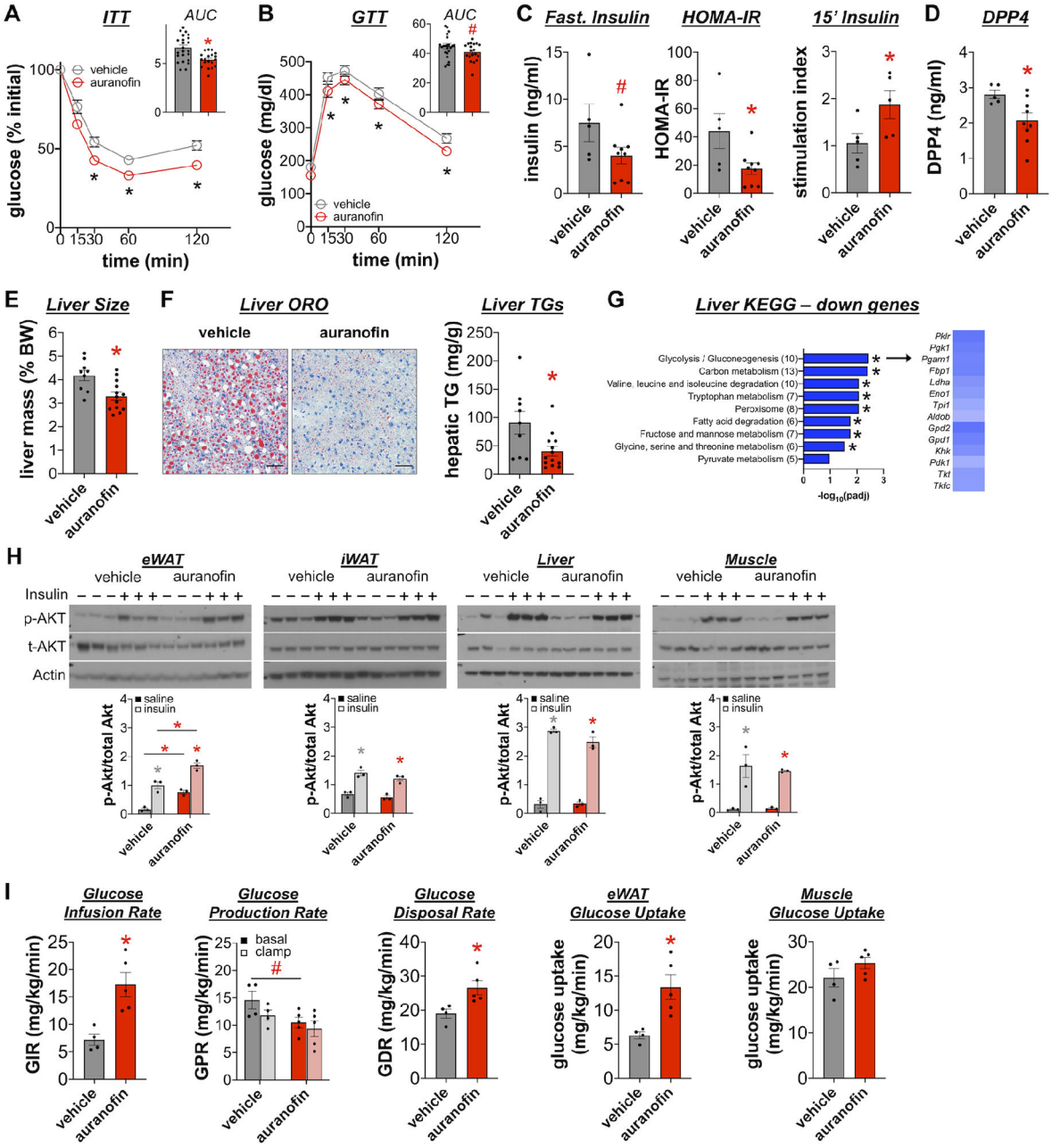

Figure 2. Auranofin improves insulin sensitivity in obese mice.

Mice fed high fat diet (HFD) for 12 weeks were i.p. injected with auranofin (1 mg/kg) or vehicle for 4 weeks. **(A)** ITT and **(B)** GTT with corresponding area under the curve measurements (n=19-24/group). **(C)** Fasting serum insulin, HOMA-IR, and glucose-stimulated insulin secretion (n=5-9/group). **(D)** Fed serum DPP4 (n=5-9/group). **(E)** Liver size (n=9-13/group), **(F)** Oil Red O (ORO) staining of liver sections and liver triglycerides (n=9-13/group), scale=100 μm. **(G)** KEGG pathway analysis of down-regulated genes by RNA-seq in the liver with auranofin shown as $-\log_{10}$(adj. p-value). Heatmap (right) shows $\log_2$ fold change for genes enriched in glycolysis/gluconeogenesis and fatty acid metabolism. **(H)** Immunoblots of tissue lysates from mice injected with insulin five minutes,

probed for p-Akt (Ser473) and total Akt followed by densitometry. Hyperinsulinemic-euglycemic clamp (n=4-5/group): **(I)** Glucose infusion rate (GIR), glucose production rate (GPR) during basal (dark bars) and clamp (light bars), glucose disposal rate (GDR), and glucose uptake in eWAT and gastrocnemius muscle (muscle).

All data are mean ± SEM. *$p<0.05$, #$p<0.10$ by two-way ANOVA with Tukey's multiple comparison test (**A**; **B**; **H**; **I**, GPR) and unpaired t-test (**A and B**, AUC; **C-F**; **I**, GDR and glucose uptake).

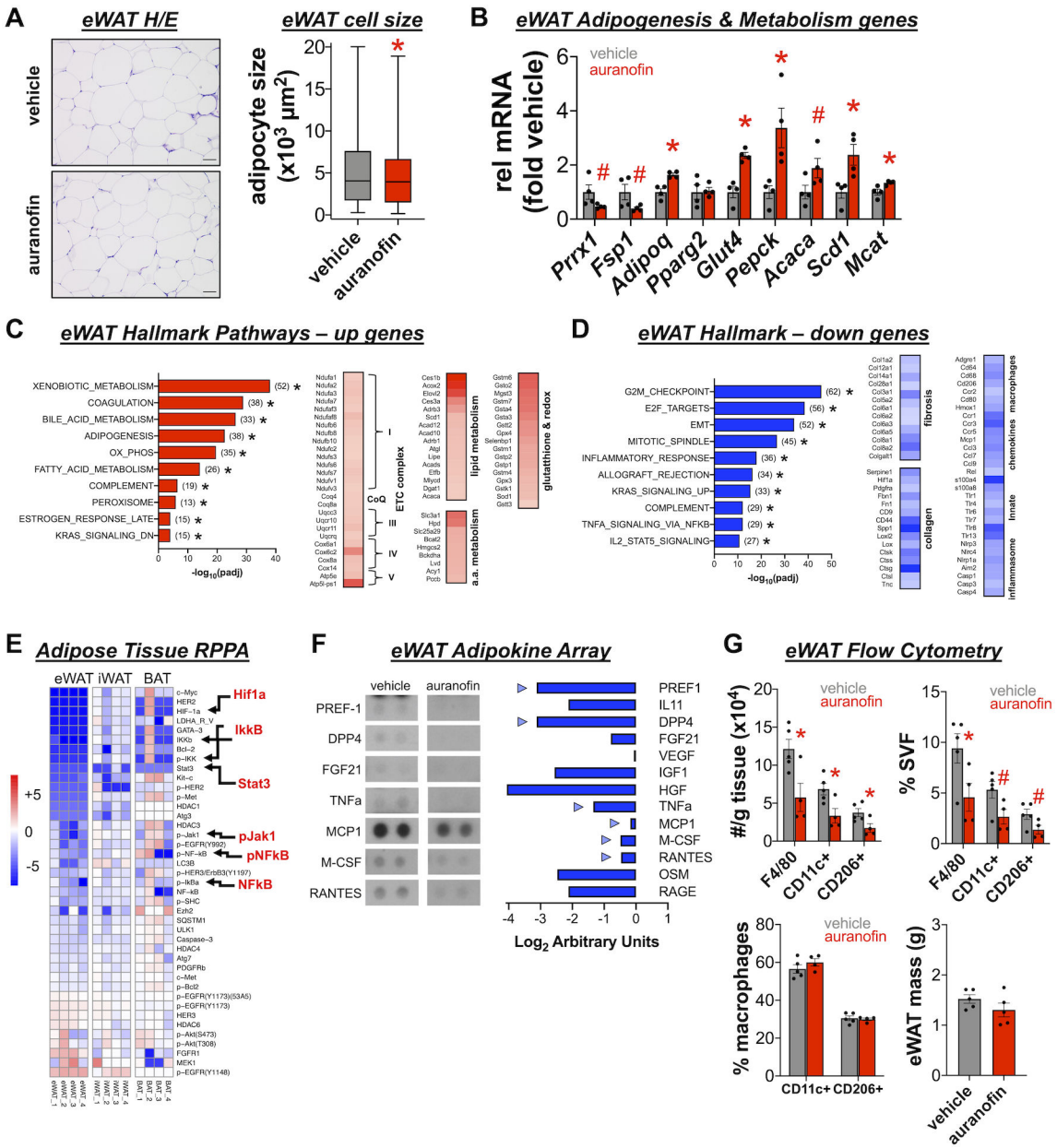

Figure 3. Auranofin expands eWAT in obese wild-type mice.

Mice fed high fat diet (HFD) for 12 weeks were i.p. injected with auranofin (1 mg/kg) or vehicle for 4 weeks. **(A)** eWAT H&E and mean adipocyte size (µm^2) across four fields of view (n=3/group), scale=50 µm. **(B)** Expression of adipogenesis and metabolism genes in eWAT. Hallmark pathway analysis of **(C)** upregulated and **(D)** down-regulated genes by RNA-seq in the eWAT shown as $-\log_{10}$(adj. p-value). Heatmaps show $\log_2$ fold change for **(C)** up genes enriched in mitochondrial complexes, lipid and amino acid metabolism, glutathione catabolism and **(D)** down genes enriched in collagen, fibrosis, and inflammation. **(E)** Reverse phase protein array (RPPA) analysis on WAT and BAT shown as $\log_2$ fold change auranofin/vehicle. **(F)** eWAT protein lysates (pooled n=4/group) incubated with adipokine arrays and quantified for relative abundance as $\log_2$ fold change auranofin/

vehicle. **(G)** eWAT total (F4/80+), M1-like (CD11c+), and M2-like (CD206+) macrophages quantified by flow cytometry (n=4-5 mice/group) with eWAT mass.

All data are mean ± SEM. *p<0.05, #p<0.10 by Mann-Whitney test (**A**), unpaired t-test (**B**; **E**, eWAT probes; **G**, eWAT mass), and two-way ANOVA with Tukey's multiple comparisons test (**G**)

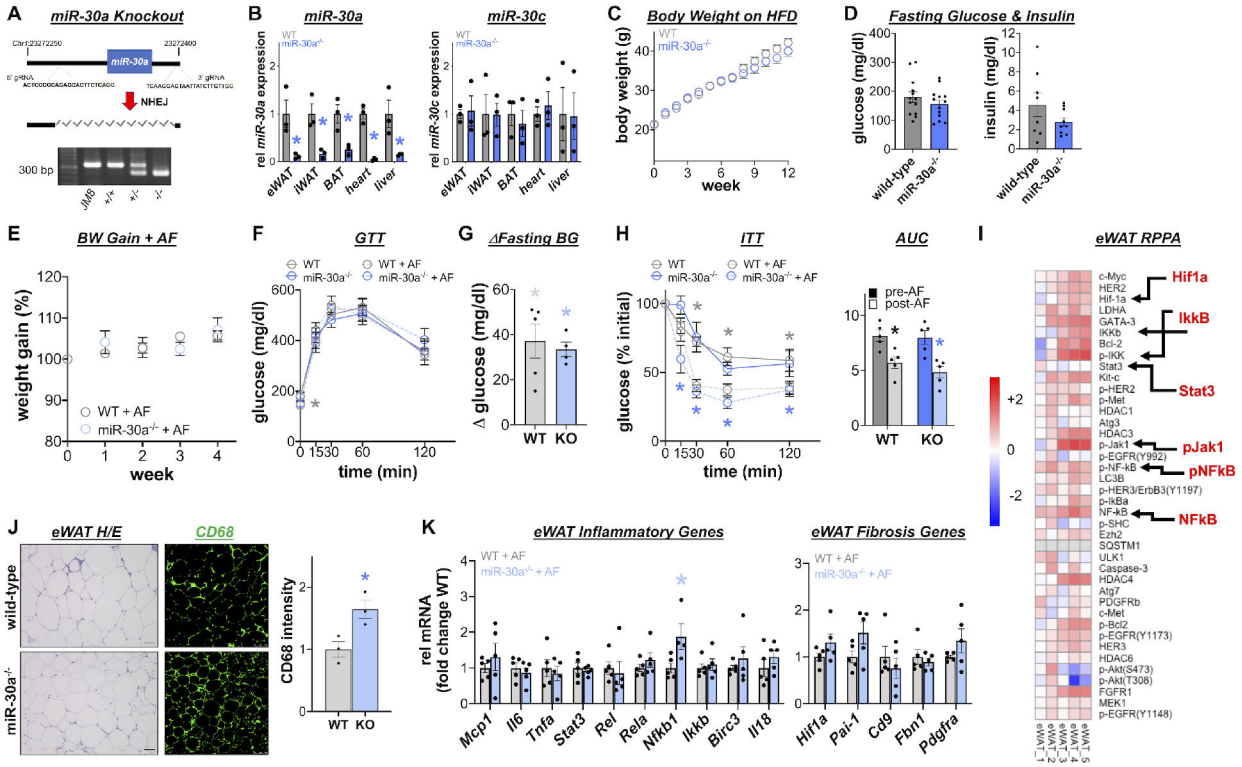

Figure 4. The metabolic effects of auranofin occur independently of *miR-30a*.

(A) Guide RNAs (gRNA) flanked a 1 kb genomic region containing *miR-30a.* Non-homologous end-joining (NHEJ) generated *miR-30a*$^{-/-}$ (KO). PCR genotyping of the targeted loci in genomic DNA from wild-type (+/+), *miR-30a*$^{+/-}$, *miR-30a*$^{-/-}$ mice or ES cells (JM8). **(B)** qPCR of *miR-30a* and *miR-30c* (six month old *miR-30a*$^{-/-}$ and littermate controls, n=3/group). **(C)** Body weight during high fat diet (HFD) for 12 weeks (n=21-22 mice/group). **(D)** Fasting glucose (n=13/group) and insulin levels (n=8-9/group). HFD-fed wild-type and *miR-30a*$^{-/-}$ were i.p. injected with auranofin (AF, 1 mg/kg) for 4 weeks. **(E)** Body weight gain of HFD wild-type and *miR-30a*$^{-/-}$ mice during auranofin treatment. **(F)** GTT and **(G)** changes (Δ) in fasting glucose after auranofin (n=4-5/group). **(H)** ITT and corresponding area under the curve measurements (n=5/group). Asterisks (gray-WT, blue-KO) indicate pre- and post- auranofin changes for each genotype. **(I)** Reverse phase protein array (RPPA) on eWAT of untreated obese wild-type and *miR-30a*$^{-/-}$ mice shown as $\log_2$ fold change KO/wild-type. **(J)** H&E stained eWAT (scale=50 μm) and immunofluorescent labeling of CD68 with quantification (five images/mouse; n=3/group; scale=100 μm). **(K)** Expression of inflammatory and fibrosis genes in eWAT after auranofin treatment.

All data are mean ± SEM. *p<0.05 by upaired t-test (**B**; **D**; **G**, vs ΔBG=0 ; **I-K**) and two-way ANOVA with Tukey's multiple comparisons test (**C**; **E**; **F**; pre- and post-AF, **H**)

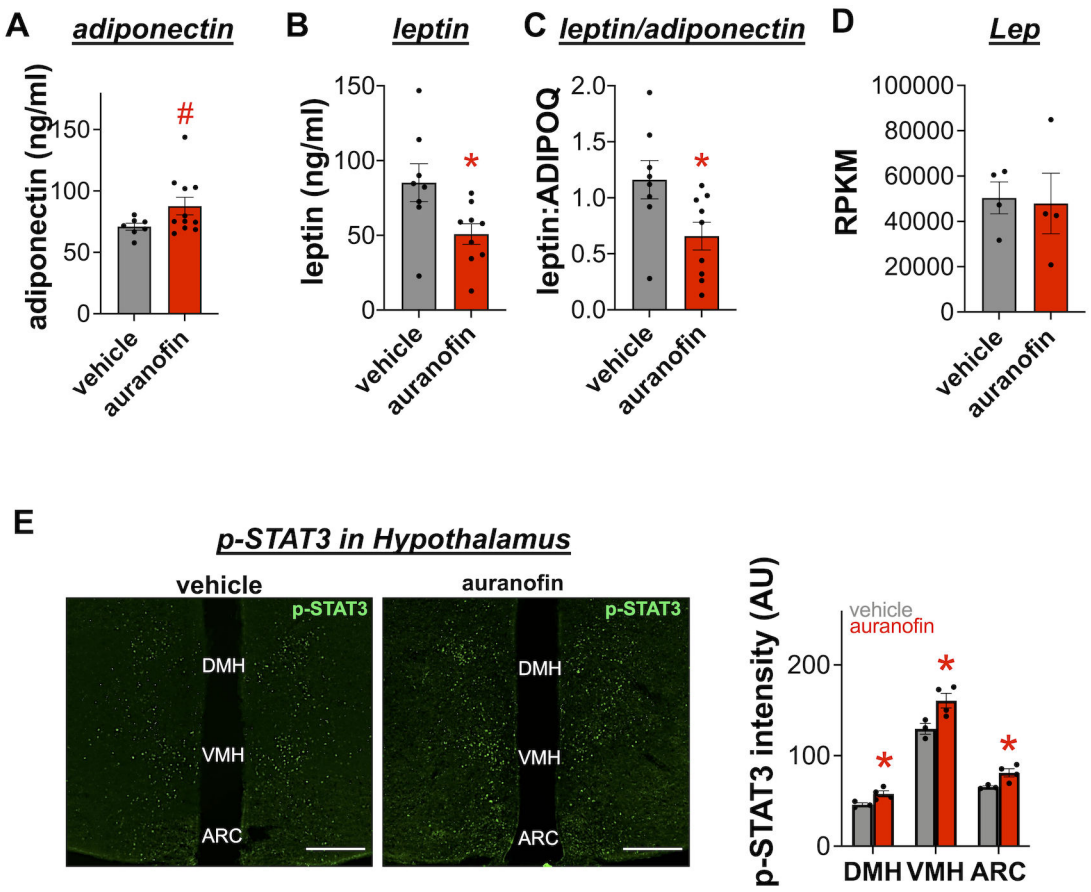

Figure 5. Auranofin lowers serum leptin levels in obese wild-type mice.

(A) Fed serum adiponectin, **(B)** leptin and **(C)** corresponding leptin to adiponectin ratio for WT+HFD (n=8-12/group). **(D)** eWAT *Lep* in wild-type mice treated with vehicle or auranofin on HFD (n=4/group). RNA-Seq data shown as reads per kb million (RPKM). **(E)** The hypothalamus was stained and quantified for p-STAT3 (n=4/group) within the dorsal medial hypothalamus (DMH), ventral medial hypothalamus (VMH) and arcuate (ARC) nuclei of HFD mice treated with auranofin (1 mg/kg), scale=200 μm.

All data are mean ± SEM. *p<0.05 by unpaired t-test (**A-D**) and two-way ANOVA with Tukey's multiple comparisons test (**E**)

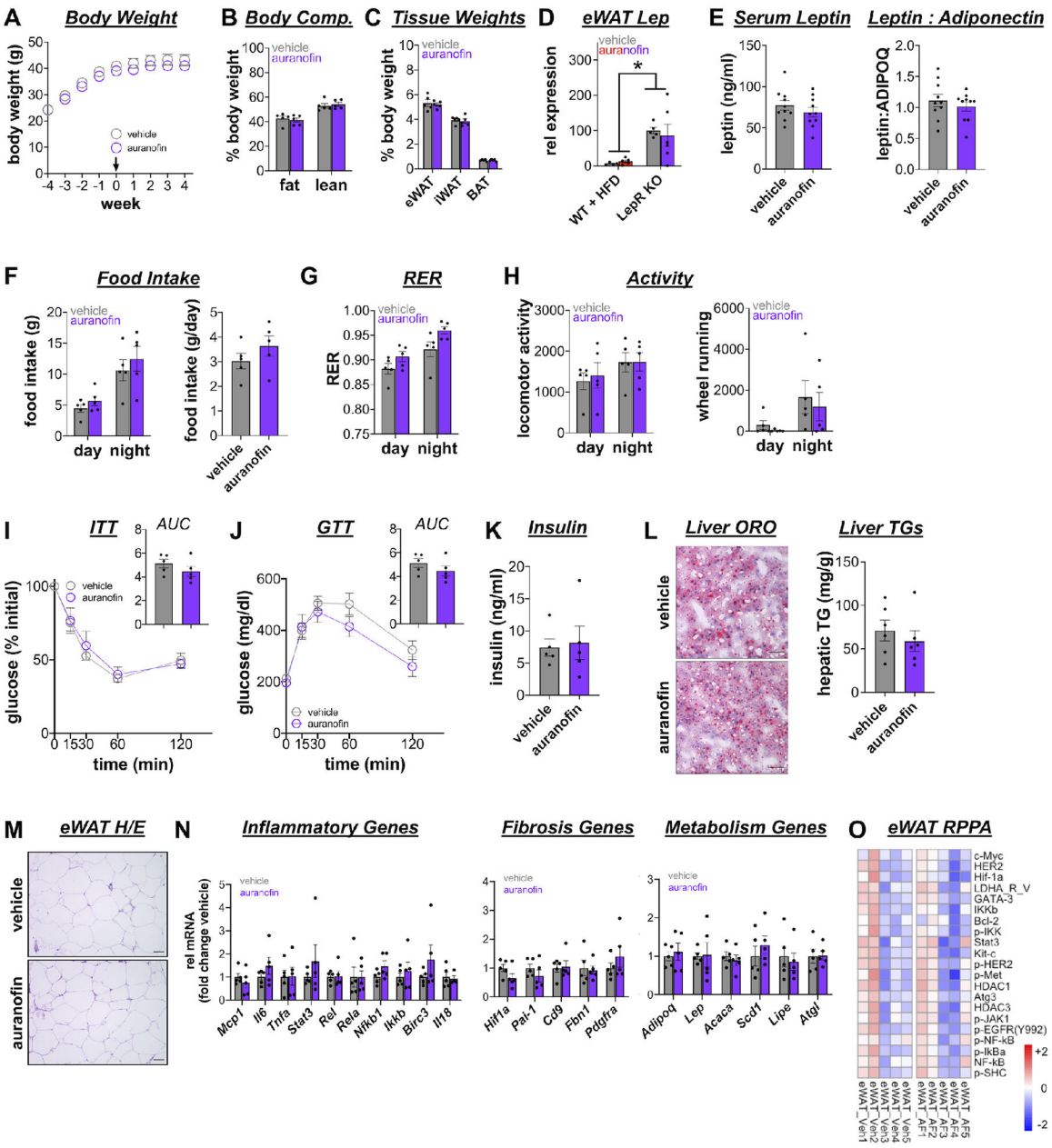

Figure 6. Genetic hyperleptinemia causes auranofin resistance.

Tamoxifen treatment induced *LepR* deletion and obesity in *Ubc-Cre;LepR*$^{lp/lp}$ (*LepR KO*) mice. After four weeks, *LepR KO* mice were i.p. injected with auranofin (1 mg/kg) or vehicle for 4 weeks (n=5/group). **(A)** Body mass during treatments. **(B)** Body composition and **(C)** tissue weights at necropsy (n=5/group). **(D)** eWAT *Lep* in wild-type mice treated with auranofin on high fat diet (WT+HFD; n=4/group) and *LepR KO* (n=5/group). **(E)** Fed serum leptin and corresponding leptin to adiponectin ratio (n=10/group). Mice were individually housed in CLAMS cages for 6 days (n=5/group). Averaged data during dark/light periods for **(F)** food intake, **(G)** RER, **(H)** locomotor activity and wheel running. **(I)** ITT and **(J)** GTT with corresponding area under the curve measurements. **(K)** Fasting serum insulin (n=5/group). **(L)** Oil Red O (ORO) staining of liver sections (scale=100 μm)

and liver triglycerides (TGs) (n=6/group). **(M)** eWAT H&E; scale=50 μm. **(N)** Expression of inflammatory, fibrosis and metabolism genes in eWAT (n=5/group). **(O)** Reverse phase protein array on eWAT of *LepR KO* mice shown as $\log_2$ fold change auranofin/vehicle. All data are mean ± SEM. *p<0.05, #p<0.1 by two-way ANOVA with Tukey's multiple comparison test (**A**; **B**; **D**; **G**, day/night food intake; **I**; **J**), ANCOVA with lean mass as a co-variate (**G**; **H**), and unpaired t-test (**C**; **E**; **F**, cumulative food intake; **I and J**, AUC; **L**; **N**; **O**)

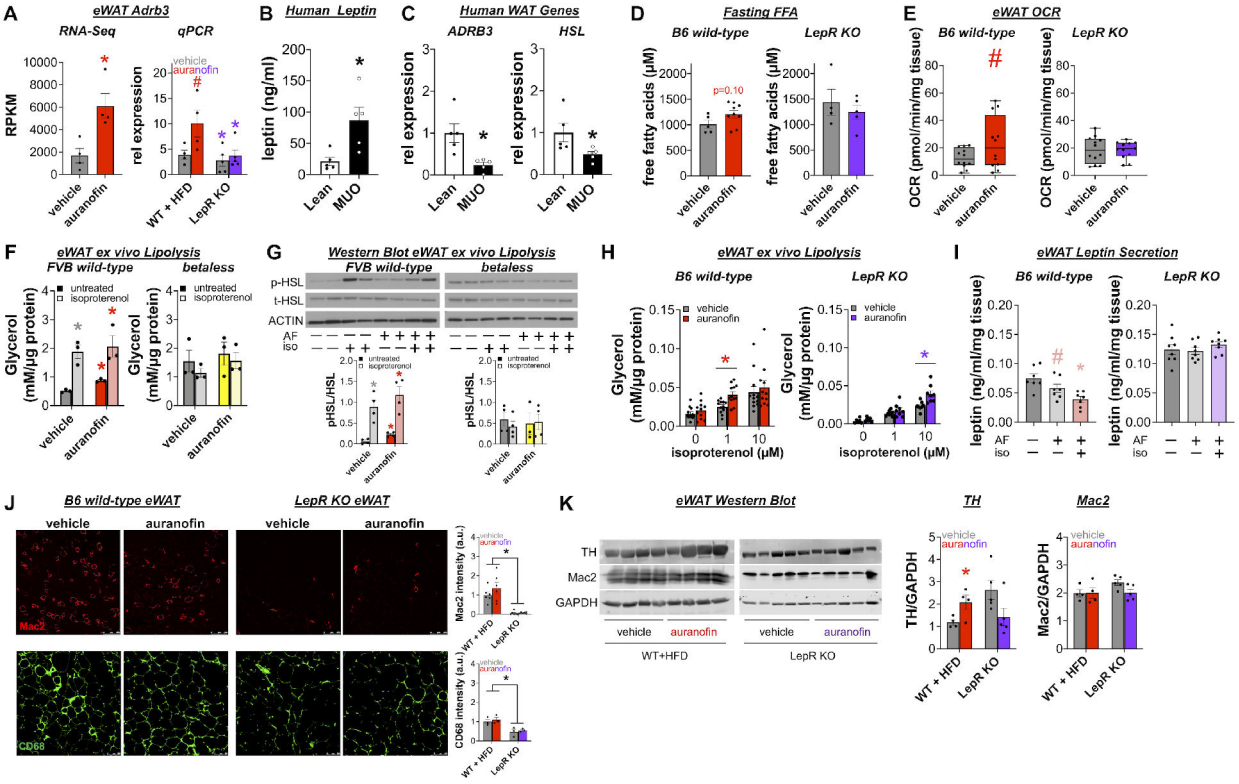

Figure 7. Auranofin restores eWAT lipolytic competence.

(A) eWAT *Adrb3* in wild-type mice fed high fat diet (WT+HFD, n=4/group) and *LepR KO* mice (n=5/group) treated with auranofin (1 mg/kg) or vehicle. RNA-Seq data shown as reads per kb million (RPKM). **(B)** Serum leptin and **(C)** *ADRB3* and *HSL* expression in subcutaneous WAT of lean and obese persons (n=5/group). **(D)** Fasting free fatty acids (WT+HFD vehicle n=5, auranofin n=9; *LepR KO* vehicle n=4, auranofin n=5). **(E)** eWAT ex vivo Oxygen consumption rate (OCR, n=12/group) after 100 nM auranofin or vehicle (DMSO). **(F)** Glycerol release from wild-type and beta-less (*Adrb1/Adrb2/Adrb3 KO*) eWAT cultured ex vivo with 100 nM auranofin or vehicle (DMSO) +/− isoproterenol (10 μM) for 2 hours (n=3/group). **(G)** Immunoblots of eWAT lysates from **(F)** probed and quantified (n=4/group) for phospho-HSL and total HSL. **(H)** Glycerol release from eWAT 2 hours after 100 nM auranofin or vehicle (DMSO) and isoproterenol (WT+HFD n=12/group; *LepR KO* n=8/group). **(I)** eWAT leptin secretion into the media two hours after vehicle, isoproterenol (1 μM), or isoproterenol (1 μM) plus 100 nM auranofin (n=7/group). **(J)** Immunofluorescent staining and quantification of macrophages using Mac2 (n=6/group, scale=250 μm) and CD68 (n=3/group, scale=100 μm). **(K)** Immunoblots of eWAT lysates probed for tyrosine hydroxylase (TH) with corresponding densitometry.

All data are mean ± SEM. *p<0.05, #p<0.10 by unpaired t-test (**A,** RNA-Seq; **B-E**), one-way ANOVA with Tukey's multiple comparisons test (**I**), and two-way ANOVA with Tukey's multiple comparisons test: (**A**, qPCR; **F**; **G**, pHSL/HSL; **H**; **J**; **K**)

KEY RESOURCES TABLE

REAGENT or RESOURCE	SOURCE	IDENTIFIER
Antibodies		
Rabbit monoclonal p-AKT (Ser473) (D9E)	Cell Signaling	4060; RRID:AB_2315049
Rabbit monoclonal pan AKT (C67E7)	Cell Signaling	4691; RRID:AB_915783
Rabbit polyclonal adiponectin	GeneTex	GTX112777; RRID:AB_2885323
Mouse monoclonal Beta actin (AC-15)	Sigma-Aldrich	A5441; RRID:AB_476744
Rabbit polyclonal HSP90	GeneTex	GTX110089; RRID:AB_1950529
Armenian hamster monoclonal CD11c (N418)	ThermoFisher	12-0114-82; RRID:AB_465552
Rat monoclonal CD206 (MR5D3)	Bio-Rad	MCA2235F; RRID:AB_324594
Rat monoclonal CD45 (30-F11)	ThermoFisher	17-0451-82; RRID:AB_469392
Rat monoclonal F4/80 (BM8)	ThermoFisher	45-4801-82; RRID:AB_914345
Rabbit polyclonal p-HSL (Ser563)	Cell Signaling	4139; RRID:AB_2135495
Rabbit polyclonal total HSL	Cell Signaling	4107; RRID:AB_2296900
Rat monoclonal Galectin-3 (MAC2) (M3/38)	eBioscience	13-5301-82; RRID:AB_837113
Rat monoclonal Galectin-3 (MAC2) (M3/38)	Novus Biologicals	NBP1-43313; RRID:AB_10006681
Rabbit monoclonal GAPDH (14C10)	Cell Signaling	2118; RRID:AB_561053
Guinea pig Perilipin 1	Progen	GP-29; RRID:AB_2892611
Rabbit polyclonal Tyrosine hydroxylase	Pel-Freez Biologicals	P40101-150; RRID:AB_2617184
Rabbit monoclonal pSTAT3 (Tyr705) (D3A7)	Cell Signaling	9145; RRID:AB_2491009
Mouse monoclonal CD68 (KP1)	Invitrogen	MA5-13324; RRID:AB_10987212
Donkey anti-mouse IgG Alexa Fluor 488	Jackson ImmunoResearch Labs	715-545-151; RRID:AB_2341099
Goat anti-rabbit IgG Alexa Fluor 488	ThermoFisher	A-11034; RRID:AB_2576217
Donkey anti-rat Alexa Fluor 647	Jackson ImmunoResearch Labs	712-606-153; RRID:AB_2340696
Donkey anti-guinea pig IgG Alexa Fluor 647	Jackson ImmunoResearch Labs	706-605-148; RRID:AB_2340476
IRDye 800CW donkey anti-rabbit IgG	Li-Cor	925-32213; RRID AB_2715510
IRDye 680RD donkey anti-mouse IgG	Li-Cor	925-68072; RRID AB_2814912
Bacterial and virus strains		
Biological samples		
Human subcutaneous preadipocytes	Zen-Bio Inc.	#SL0065
Chemicals, peptides, and recombinant proteins		
Auranofin	Sigma-Aldrich	A6733
Tamoxifen	MP Biomedicals	156738
T-PER Tissue Protein Extraction Reagent	ThermoFisher	78510
Halt Protease and Phosphatase Inhibitor Cocktail	ThermoFisher	78440
4′,6-diamidino-2-phenylindole (DAPI)	Sigma-Aldrich	D8417
MitoTracker Red CMX-ROS	ThermoFisher	M7512
LipidTOX	Life Technologies	H34475

REAGENT or RESOURCE	SOURCE	IDENTIFIER
DAPI Fluoromount-G	VWR	0100-20
IRDye 680RD Streptavidin	LI-COR	926-68079
Tissue-Tek OCT compound	Sakura Finetek	4583
Formaldehyde	ThermoFisher	28908
Collagenase type I	Worthington Biochemical Corp	LS004194
Collagenase type I	Roche	17100-017
Dispase II	Sigma-Aldrich	D4693
Isobutylmethylxanthine (IBMX)	Sigma-Aldrich	13347
Rosiglitazone	Cayman Chemical Co	71740
Dexamethasone	Tocris Biosciences	1126
Insulin	Sigma-Aldrich	I5500
3,3′,5-Triiodo-L-thyronine (T_3)	Sigma-Aldrich	T-074
DMSO	Sigma-Aldrich	D2660
Polyethylene glycol 400	Affymetrix	19957
Ethanol absolute 200 proof	Fisher Scientific	BP2818
10% Neutral buffered formalin	Fisher Chemical	SF100-4
DMEM/F-12, GlutaMAX	ThermoFisher	10565-018
Fetal Bovine Serum	VWR	97068-085
Penicillin-Streptomycin	Gibco	15140-122
Sodium pyruvate	Gibco	11360-070
L-glutamine	Gibco	25030-081
Seahorse XF assay medium modified DMEM	Agilent	102365-100
Isoproterenol	Cayman Chemical	15592
2-deoxy-D-glucose, [1-^{14}C]	PerkinElmer	NEC720A050UC
Glucose, D-[2-^{3}H]	PerkinElmer	NET238C001MC
Critical commercial assays		
Rat/Mouse Insulin ELISA	Millipore	EZRMI-13K
Mouse Leptin ELISA kit	Crystal Chem	90030
Adiponectin Mouse ELISA Kit	ThermoFisher	KMP0041
DPPIV (DPP4/CD26) Mouse ELISA Kit	ThermoFisher	EMDPP4
Proteome Profiler Mouse Adipokine Array Kit	R&D Systems	ARY013
Triglycerides Reagent	ThermoFisher	TR22421
Glycerol Assay kit	Sigma-Aldrich	MAK117
Serum/Plasma Fatty Acid Detection Kit	Zen-Bio Inc.	sfa-1
Deposited data		
RNA-seq data	This paper	GEO: GSE202935
Experimental models: Cell lines		
Experimental models: Organisms/strains		

REAGENT or RESOURCE	SOURCE	IDENTIFIER
Mouse: C57/Bl6J	BCM Center for Comparative Medicine	N/A
Mouse: FVB	BCM Center for Comparative Medicine	N/A
Mouse: Ubc-CreERT2;LepR-lp/lp	Cox et al. 2016	N/A
Mouse: B6.Cg-Lep^{ob}/J	Jackson Laboratory	000632; RRID:IMSR_JAX:000632
Beta-less (bAR1, bAR2, bAR3 knockout mice)	Bachmann et al. 2002; Xu et al. 2014	N/A
miR-30a $^{-/-}$	This paper	N/A
Oligonucleotides		
Primers for qPCR, see Table S2	This paper	N/A
sgRNA sequence: miR-30a upstream ACTCCCGCAGAGCACTTCTCAGG	This paper	N/A
sgRNA sequence: miR-30a downstream TCAAGGAGTAATTATCTTGTTGG	This paper	N/A
Primer: miR-30a forward GCATCGAGGCTTTGCAGTTT	This paper	N/A
Primer: miR-30a reverse TGCACAGGAAGAACACTTCTGT	This paper	N/A
Recombinant DNA		
Software and algorithms		
Fiji	Schindelin et. al. 2012	https://imagej.net/software/fiji/
ImageJ with Adiposoft plugin	CIMA, University of Navarra	https://imagej.net/plugins/adiposoft
Prism 9	GraphPad	https://www.graphpad.com/
CalR	Palmer et al. 2017	https://calrapp.org/
STAR	Dobin et al., 2013	https://github.com/alexdobin/STAR
DESeq2	Love et al., 2014	https://github.com/mikelove/DESeq2
GSEA	Subramanian et al., 2005	https://www.gsea-msigdb.org/gsea/index.jsp
GenePix Pro 7.0 Microarray Acquisition & Analysis Software	Molecular Devices	https://www.moleculardevices.com
Other		
4-12% Bis-Tris NuPage gels	Life Technologies	NP0321Box
Immobilon-P Transfer Membranes	Millipore	IPVH00010
Direct-zol RNA MiniPrep kit	Zymo Research	R2051
qScript	QuantBio	95048-100
Sso-Advanced Universal Probes Supermix	Bio-Rad	175284
TaqMan Advanced miRNA cDNA Synthesis	ThermoFisher	A28007
TaqMan Advanced miRNA Assays	ThermoFisher	A25576
TaqMan Gene Expression Assays (FAM)	ThermoFisher	4331182
NEBNext Ultra II DNA library prep kit	New England Biolabs	E7645S
Seahorse XF24 Islet Capture FluxPak	Agilent	103518-100
Seahorse XF24 FluxPak	Agilent	102342-100
Seahorse XF24 V7-PS cell culture microplates	Agilent	100777-004

REAGENT or RESOURCE	SOURCE	IDENTIFIER
Seahorse XF Cell Mito Stress Test Kit	Agilent	103010-100
60% high fat diet	Bio-Serv	S3282
Precision Count Beads	BioLegend	424902